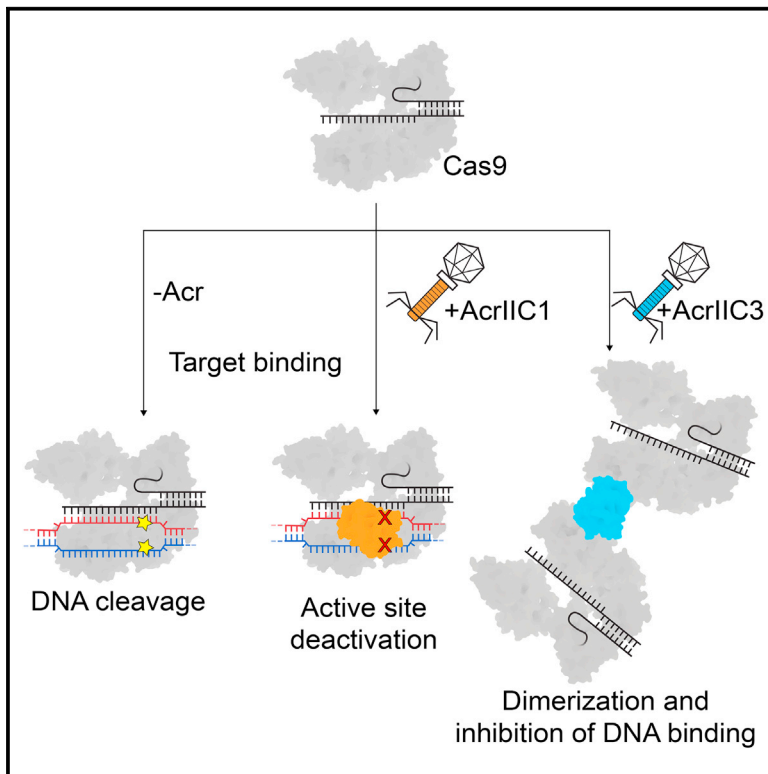


A Broad-Spectrum Inhibitor of CRISPR-Cas9

Graphical Abstract



Authors

Lucas B. Harrington, Kevin W. Doxzen, Enbo Ma, ..., Alan R. Davidson, Karen L. Maxwell, Jennifer A. Doudna

Correspondence

doudna@berkeley.edu

In Brief

The mechanisms by which two different anti-CRISPR proteins inhibit Cas9 may provide CRISPR-based regulatory tools to allow DNA binding while preventing cleavage.

Highlights

- Phage-encoded anti-CRISPRs (Acrs) inhibit CRISPR-Cas9 through unique mechanisms
- AcrIIC1 controls genome editing by diverse Cas9 orthologs
- AcrIIC1 binding disables Cas9's nucleases without impacting DNA binding
- AcrIIC3 promotes dimerization of Cas9 and prevents DNA binding



A Broad-Spectrum Inhibitor of CRISPR-Cas9

Lucas B. Harrington,^{1,12} Kevin W. Doxzen,^{2,12} Enbo Ma,¹ Jun-Jie Liu,^{1,3} Gavin J. Knott,¹ Alireza Edraki,⁴ Bianca Garcia,⁵ Nadia Amrani,⁴ Janice S. Chen,¹ Joshua C. Cofsky,¹ Philip J. Kranzusch,^{6,7} Erik J. Sontheimer,⁴ Alan R. Davidson,^{5,8} Karen L. Maxwell,⁵ and Jennifer A. Doudna^{1,2,3,9,10,11,13,*}

¹Department of Molecular and Cell Biology, University of California, Berkeley, Berkeley, CA 94720, USA

²Biophysics Graduate Group, University of California, Berkeley, Berkeley, CA 94720, USA

³Department of Chemistry, University of California, Berkeley, Berkeley, CA 94720, USA

⁴RNA Therapeutics Institute, Program in Molecular Medicine, University of Massachusetts Medical School, Worcester, MA 01605, USA

⁵Department of Biochemistry, University of Toronto, Toronto, ON M5S 1A8, Canada

⁶Department of Microbiology and Immunobiology, Harvard Medical School, Boston, MA 02115, USA

⁷Department of Cancer Immunology and Virology, Dana-Farber Cancer Institute, Boston, MA 02115, USA

⁸Department of Molecular Genetics, University of Toronto, Toronto, ON M5S 1A8, Canada

⁹Howard Hughes Medical Institute, University of California, Berkeley, Berkeley, CA 94720, USA

¹⁰Innovative Genomics Institute, University of California, Berkeley, Berkeley, CA 94720, USA

¹¹MBIB Division, Lawrence Berkeley National Laboratory, Berkeley, CA 94720, USA

¹²These authors contributed equally

¹³Lead Contact

*Correspondence: doudna@berkeley.edu

<http://dx.doi.org/10.1016/j.cell.2017.07.037>

SUMMARY

CRISPR-Cas9 proteins function within bacterial immune systems to target and destroy invasive DNA and have been harnessed as a robust technology for genome editing. Small bacteriophage-encoded anti-CRISPR proteins (Acrs) can inactivate Cas9, providing an efficient off switch for Cas9-based applications. Here, we show that two Acrs, AcrIIC1 and AcrIIC3, inhibit Cas9 by distinct strategies. AcrIIC1 is a broad-spectrum Cas9 inhibitor that prevents DNA cutting by multiple divergent Cas9 orthologs through direct binding to the conserved HNH catalytic domain of Cas9. A crystal structure of an AcrIIC1-Cas9 HNH domain complex shows how AcrIIC1 traps Cas9 in a DNA-bound but catalytically inactive state. By contrast, AcrIIC3 blocks activity of a single Cas9 ortholog and induces Cas9 dimerization while preventing binding to the target DNA. These two orthogonal mechanisms allow for separate control of Cas9 target binding and cleavage and suggest applications to allow DNA binding while preventing DNA cutting by Cas9.

INTRODUCTION

CRISPR systems provide bacteria and archaea with adaptive immunity against foreign DNA and RNA (Barrangou et al., 2007; Brouns et al., 2008; Marraffini and Sontheimer, 2008). To initiate immunity, Cas9s integrate fragments of invading DNA into the host genome at the CRISPR locus, where they serve as transcription templates for the synthesis of RNA that directs Cas nucleases to cleave infectious nucleic acids (Garneau et al., 2010; Hale et al., 2009). Class 2 CRISPR systems

are streamlined versions that require only a single protein to target foreign DNA or RNA (Makarova et al., 2015; Shmakov et al., 2017). CRISPR-Cas9, the most abundant and diverse of class 2 CRISPR proteins, exists in three subtypes, of which type IIA and IIC are more common compared to the relatively rare type IIB (Chylinski et al., 2014; Shmakov et al., 2017). The programmable nature of Cas9 has made it a powerful tool for gene editing and genomic modulation in a wide range of organisms.

In response to these robust prokaryotic immune systems, phages have evolved proteins that bind to and inactivate Cas proteins as they search for foreign nucleic acids (Bondy-Denomy et al., 2013, 2015; Pawluk et al., 2014). Although only a small number of these anti-CRISPRs (Acrs) have been discovered to date, phylogenetic analysis suggests that Acrs are widespread and likely play a significant role in the evolution of Cas proteins (van Houte et al., 2016; Pawluk et al., 2016a). In addition to their native functions, Acrs that inhibit Cas9 nucleases allow for control of Cas9 in genome-editing applications (Pawluk et al., 2016b; Rauch et al., 2017). Specifically, three unique Acrs that target the type IIC Cas9 from *Neisseria meningitidis* (NmeCas9) have been identified (AcrIIC1, 2, and 3) along with four that target select type IIA Cas9 orthologs (AcrIIA1, 2, 3, and 4). Whereas some of these Acrs have been shown to inhibit NmeCas9 and SpyCas9 in mammalian cells (Pawluk et al., 2016b; Rauch et al., 2017), their ability to inactivate other Cas9 orthologs used for genome editing remains unknown. Understanding this specificity as well as the mechanisms by which they disable Cas9 will be critical for their successful deployment as modulators of Cas9 in human and other cell types. Apart from applications, this mechanistic information is also fundamental to understanding how these Acrs have evolved to target distinct Cas9 orthologs and what evolutionary pressures they impose on CRISPR systems.

Here, we investigated the inactivation of Cas9 by AcrIIC1 and AcrIIC3, uncovering unique mechanisms for both. We focused

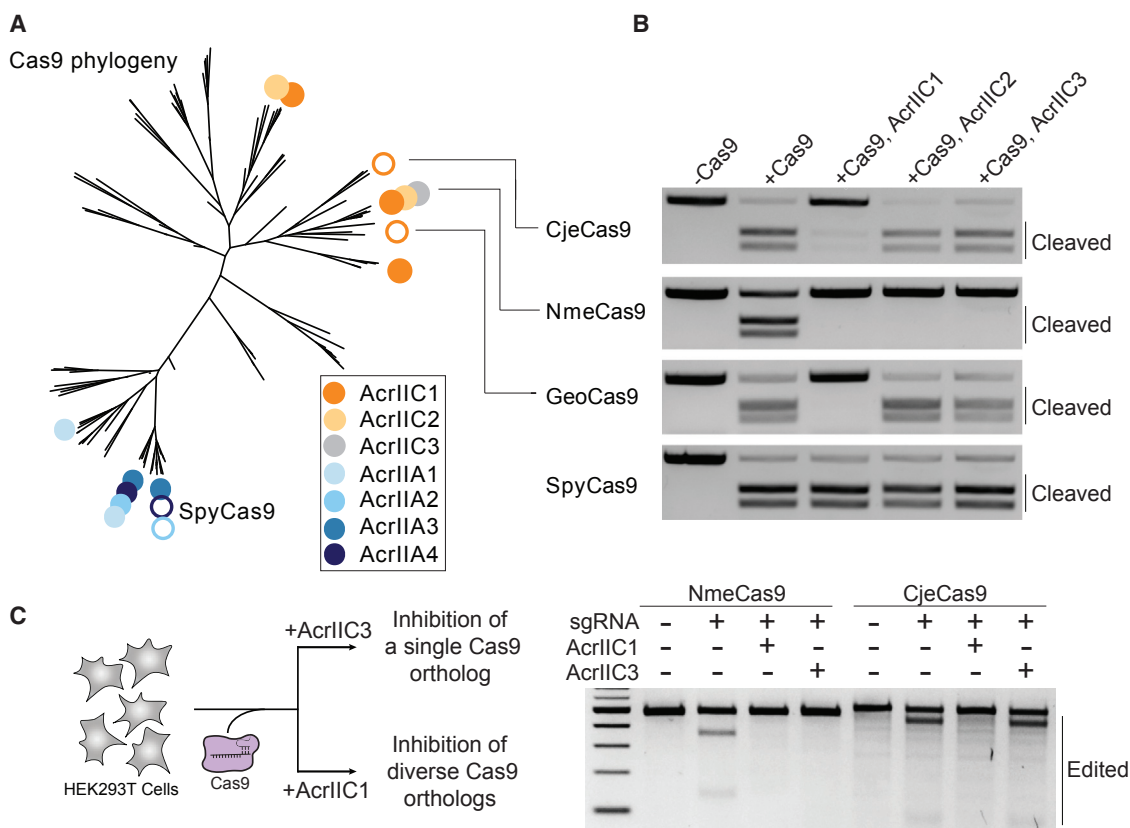


Figure 1. AcrIIC1 Inhibits Diverse Cas9 Orthologs, whereas AcrIIC2 and AcrIIC3 Are Highly Specific

(A) Unrooted phylogenetic tree of Cas9. Cas9 orthologs targeted by Acrs are indicated with circles at ends of branches (closed circles, Cas9 orthologs naturally targeted by an Acr; open circles, Cas9 orthologs that have been shown experimentally to be inhibited by an Acr but without naturally occurring AcrIIC1 orthologs). For branches containing multiple Acrs of a given type, only one circle is shown for simplicity (phylogeny adapted from Burstein et al., 2017).

(B) DNA cleavage assays conducted by various Cas9 orthologs in the presence of AcrIIC1, AcrIIC2, and AcrIIC3 (–Cas9, no Cas9 added; +Cas9, Cas9 and sgRNA added; Cje, *Campylobacter jejuni*; Nme, *Neisseria meningitidis*; Geo, *Geobacillus stearothermophilus*; Spy, *Streptococcus pyogenes*).

(C) (Left) Cartoon depicting experiment to test inhibition of Cas9 orthologs by AcrIIC1 in HEK293 cells. (Right) T7E1 assay analyzing indels produced by CjeCas9 and NmeCas9 shows that CjeCas9 genome editing is inhibited by AcrIIC1_{Nme}, but not AcrIIC3_{Nme}.

See also Figure S1.

on these two Acrs because of their potent inhibition of NmeCas9 in human cells (Pawluk et al., 2016b). Our data show that AcrIIC1 blocks DNA cleavage by multiple Cas9 orthologs without impacting DNA binding, effectively transforming catalytically active Cas9 into catalytically inactive dCas9. This mechanism is accomplished by AcrIIC1 binding directly to the HNH nuclease domain of Cas9, obscuring the active site and restricting conformational changes required for cleavage. AcrIIC3, by contrast, inhibits only a single Cas9 ortholog by blocking DNA binding. AcrIIC3 also causes Cas9 to dimerize, possibly contributing to its ability to interfere with target recognition and suggesting a mechanism distinct from that observed for AcrIIA4 (Dong et al., 2017; Shin et al., 2017). Together, AcrIIC1 and AcrIIC3 enable either broad-spectrum or selective inhibition of Cas9 orthologs, respectively. The different mechanisms of these two Acrs allow separate control of binding to and cleavage of DNA by Cas9. Moreover, these mechanisms reveal vulnerabilities of Cas9 that are susceptible to inhibition, shedding light on the evolutionary arms race between bacteriophage and bacteria.

RESULTS

AcrIIC1 Inhibits Diverse Cas9 Orthologs

Phylogenetic analysis revealed that AcrIIC1 is part of an unusually diverse family of Acr proteins (Figure S1A). Mirroring this diversity, the bacterial genomes containing AcrIIC1 include Cas9 orthologs that span a large portion of the type IIC Cas9 tree (Figure 1A). Based on its phylogenetic distribution, we hypothesized that AcrIIC1 would be more promiscuous than other Acr proteins with respect to the Cas9 orthologs it can inhibit.

To test this idea, we conducted cleavage assays using various type IIC Cas9 orthologs previously shown to function in human cells (Esvelt et al., 2013; Harrington et al., 2017; Hou et al., 2013; Kim et al., 2017). We found that, in addition to NmeCas9, the AcrIIC1 from *Neisseria meningitidis* (AcrIIC1_{Nme}) exhibits robust inhibition of the Cas9 proteins from *Geobacillus stearothermophilus* (GeoCas9) and *Campylobacter jejuni* (CjeCas9) (Figures 1B and S1B). CjeCas9 and GeoCas9 are 36% and 42% identical to NmeCas9, respectively, and represent diverse

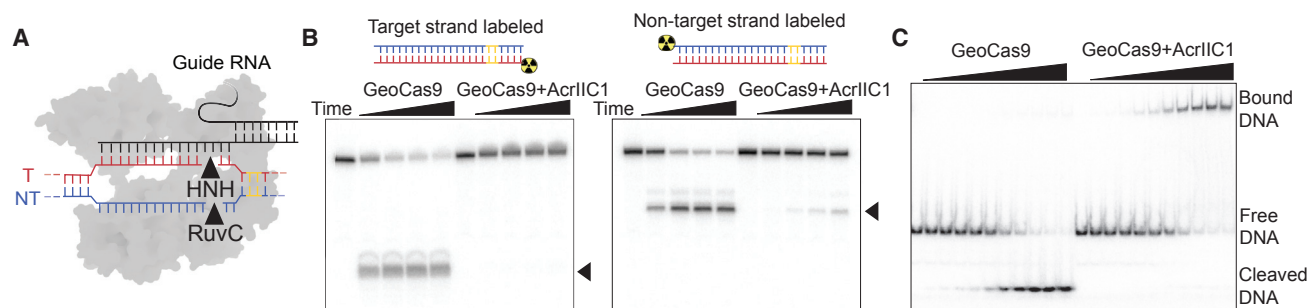


Figure 2. AcrIIIC1 Traps the DNA-Bound Cas9 Complex

(A) Cartoon of Cas9-mediated double-stranded DNA cleavage. Guide RNA (black) is duplexed to the DNA target strand (red), which is splayed from the DNA non-target strand (blue) adjacent to the PAM sequence (yellow). The HNH and RuvC nuclease domains (black triangles) cleave the target strand and non-target strand, respectively.

(B) Radiolabeled cleavage assays conducted using GeoCas9 to measure AcrIIIC1 inhibition of cleavage on the target and non-target strands. Cas9-sgRNA RNP was complexed with or without AcrIIIC1 and added to radiolabeled target DNA duplex with each strand labeled separately. The lanes for a given condition correspond to increasing time (0–30 min) from left to right. Black triangles indicate cleavage products.

(C) Analysis of GeoCas9 binding and cleavage in the presence or absence of AcrIIIC1 analyzed on a non-denaturing gel with the non-target strand labeled. GeoCas9 RNP concentration was varied in the absence or presence of excess AcrIIIC1. The top band corresponds to GeoCas9 bound to the target DNA, the middle band is free DNA, and the lower band is cleaved DNA (concentration series correspond to 0, 1, 2, 4, 8, 16, 32, 64, 128, 256, and 512 nM of GeoCas9 RNP). See also Figure S2.

branches of the type IIC Cas9 phylogeny (Figure 1A). By contrast, AcrIIIC2 and AcrIIIC3 were both highly specific for NmeCas9, having no noticeable impact on CjeCas9- or GeoCas9-catalyzed DNA cleavage (Figures 1B and S1B).

To determine whether inhibition by AcrIIIC1 can disable CjeCas9 in genome-editing applications, we transfected HEK293T cells with plasmids expressing NmeCas9, CjeCas9, or SpyCas9 and their respective single-guide RNAs (sgRNAs) in the presence or absence of a gene encoding AcrIIIC1 (Figures 1C and S1C). Similar to the biochemical cleavage assays, we observed that, in cells, CjeCas9 is inhibited by AcrIIIC1, but not by AcrIIIC3. Expressing AcrIIIC1_{Nme} or the AcrIIIC1 from *Brackiella oedipodis* (AcrIIIC1_{Boo}) resulted in efficient inhibition of CjeCas9, indicating that this promiscuity is not unique to the AcrIIIC1_{Nme} ortholog (Figure S1C). In similar cell-based assays, we found that AcrIIIC1 is also a potent inhibitor of GeoCas9 ribonucleo-protein complexes (RNPs) in mammalian cells (Figure S1D), revealing that AcrIIIC1 can also function when delivered as an expressed protein. The robust inhibition of both CjeCas9 and GeoCas9, in addition to NmeCas9, suggested that AcrIIIC1 exploits a conserved feature of the Cas9 protein.

AcrIIIC1 Traps the DNA-Bound Cas9 Complex

Acrs can potentially inhibit Cas9 proteins at multiple distinct steps, including guide RNA binding, target DNA binding, or target cleavage. To determine the step at which AcrIIIC1 inhibition occurs, we biochemically tested each of these possible mechanisms. First, we measured the binding affinity of NmeCas9 for its sgRNA in the presence and absence of AcrIIIC1 (Figure S2A) and found that RNP assembly was unaffected by AcrIIIC1. Next, we conducted equilibrium binding measurements of NmeCas9-sgRNA to its target DNA. Surprisingly, we found that NmeCas9 DNA binding was unimpeded by the presence of AcrIIIC1, indicating that AcrIIIC1 selectively blocks DNA cleavage (Figures S2B and S2C). Titrating AcrIIIC1 and AcrIIIC3 in a

cleavage assay revealed that both are capable of inhibiting NmeCas9 even at low concentrations (Figure S2D). We conducted end-labeled cleavage assays to determine whether cutting of both the target and non-target DNA strands is inhibited to the same degree (Figures 2A and 2B). Here, we found that AcrIIIC1 strongly inhibits cleavage of both DNA strands but with a subtle difference in kinetics. Although slow cleavage of the non-target DNA strand catalyzed by the RuvC active site is observed, target-strand cleavage catalyzed by the HNH domain is undetectable. These results suggested that AcrIIIC1 traps Cas9 in its DNA-bound state while inhibiting DNA cleavage. We tested this hypothesis by conducting gel shift assays using catalytically active GeoCas9 with and without AcrIIIC1. In the absence of AcrIIIC1, GeoCas9 cleaved its DNA target substrate at concentrations above ~30 nM (Figure 2C). However, when AcrIIIC1 was included in the reaction, Cas9 did not cleave the target DNA, even though DNA binding was unaffected. This remarkable mechanism is distinct from the recently studied AcrIIA2 and AcrIIA4 anti-CRISPR proteins, which function as inhibitors of DNA binding by SpyCas9 (Dong et al., 2017; Shin et al., 2017). The unique ability of AcrIIIC1 to trap Cas9 on its DNA target in a catalytically inactive state effectively transforms the wild-type Cas9 into its catalytically inactive variant dCas9 (Jinek et al., 2012).

AcrIIIC1 Binds to the HNH Domain of Cas9

The ability of AcrIIIC1 to inhibit multiple Cas9 orthologs without preventing DNA binding suggested that it targets a conserved region of Cas9 involved in DNA cleavage. To determine which region of Cas9 interacts with AcrIIIC1, we generated Cas9 truncations and tested their abilities to bind to AcrIIIC1 using size-exclusion chromatography (Figures 3A, 3B, and S3A). Although many NmeCas9 truncations were insoluble, we took advantage of the thermostable GeoCas9 (Harrington et al., 2017) to generate soluble truncations. AcrIIIC1 was able to associate

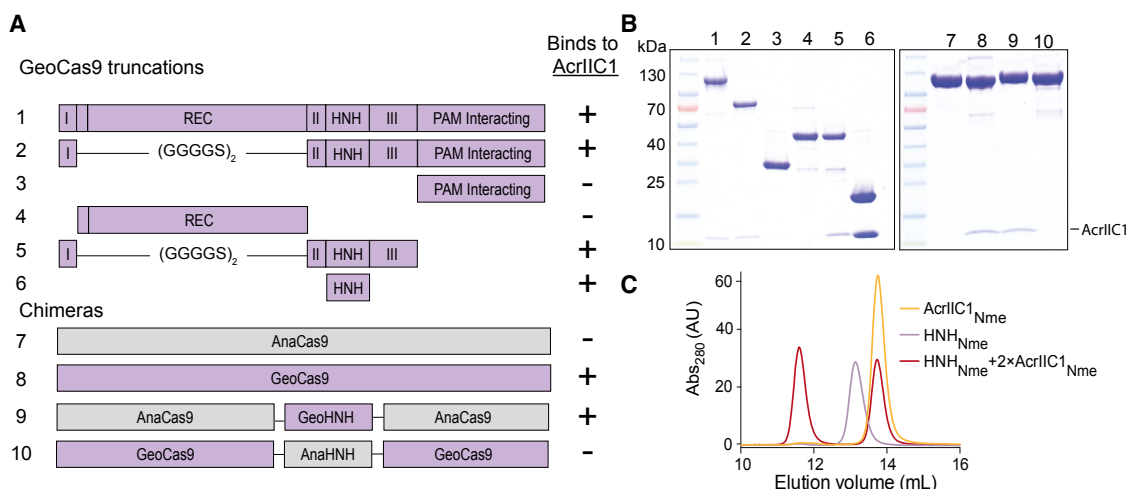


Figure 3. AcrIIIC1 Binds to Cas9 HNH Domain

(A) Domain schematics of GeoCas9 truncations and Cas9 chimeras, designed to identify the Cas9 binding interface of AcrIIIC1. Constructs 1–10 were incubated with AcrIIIC1, fractionated over an S200 size-exclusion column, and analyzed by SDS-PAGE. Constructs that bound to AcrIIIC1 are indicated with a (+), and constructs that showed no interaction are indicated with a (-). The chimeric Cas9 proteins (7–10) were generated by switching the HNH domains of a Cas9 that is not inhibited by AcrIIIC1 (AnaCas9) and a Cas9 that is inhibited (GeoCas9).

(B) Fractions from the S200 runs in Figure S3A were separated on a 4%–20% SDS-PAGE gel. Numbers above the gel correspond to the construct or chimera numbers from Figure 2A.

(C) Elution from an S75 size-exclusion column of NmeCas9 HNH domain (purple), AcrIIIC1 (orange), or the two incubated together with 2-fold excess AcrIIIC1 (red). See also Figure S3.

with GeoCas9 without either the guide RNA recognition (REC)- or protospacer adjacent motif (PAM)-interacting domains (Figure 3A), leaving the two nuclease domains as potential interacting partners. Truncating further to remove the RuvC domain allowed us to identify the HNH domain as being sufficient for AcrIIIC1 binding to Cas9 (Figures 3A, 3B, and S3A). Cas9 binding to RNA and DNA has been shown to be independent of the HNH domain (Sternberg et al., 2015; Yamada et al., 2017). In line with this, complexing of GeoCas9 with AcrIIIC1 revealed that AcrIIIC1 is able to interact with Cas9, irrespective of the presence of sgRNA or sgRNA and target DNA (Figure S3B). To determine whether AcrIIIC1 interacts specifically with the HNH domain, we exchanged the HNH domain of a Cas9 ortholog that does not interact with AcrIIIC1 (*Actinomyces naeslundii* [AnaCas9]) with an ortholog that does (GeoCas9). Here, we found that the GeoCas9 chimera containing the AnaCas9 HNH domain no longer bound to AcrIIIC1, whereas the AnaCas9 with the GeoCas9 HNH domain substitution was able to interact with AcrIIIC1 (Figures 3A, 3B, and S3C). These results indicated that the HNH domain is the primary site of interaction for AcrIIIC1.

To examine whether this interaction also occurs with NmeCas9, we purified the HNH domain of NmeCas9 and tested its ability to bind to AcrIIIC1 using size-exclusion chromatography (Figure 3C). Whereas AcrIIIC1 and the HNH domain eluted at similar volumes in isolation, applying the two proteins to the size-exclusion column together resulted in a large shift in elution volume, indicative of protein association. Importantly, the eluted HNH_{Nme}-AcrIIIC1 complex remains in the included volume of the column, indicating that the large shift is not due to aggregation. Further analysis of AcrIIIC1 binding to the NmeCas9 HNH domain

by isothermal titration calorimetry (ITC) demonstrated an equilibrium binding affinity of AcrIIIC1 6.3 ± 3.4 nM with a stoichiometry of one AcrIIIC1 for each Cas9 (Figure S3D). The HNH nuclease domain is highly conserved across all Cas9 proteins (Figure S3E) and controls cleavage of both strands of the target DNA (Dagdas et al., 2017; Sternberg et al., 2015). Although the Cas9 HNH nuclease domain is directly responsible for cleavage of the target strand of the DNA (Gasiunas et al., 2012; Jinek et al., 2012), conformational activation of the HNH domain is a prerequisite for activating cleavage of the non-target strand by the RuvC nuclease domain (Sternberg et al., 2015). The ability of AcrIIIC1 to bind to the most conserved domain of Cas9 explains its ability to robustly inhibit related Cas9 orthologs (Figure 1B) and its wide phylogenetic distribution (Figure 1A).

Structure of AcrIIIC1 Bound to the Cas9 HNH Domain

To better understand how AcrIIIC1 has evolved to bind to multiple Cas9 proteins, we determined a 1.5-Å resolution crystal structure of AcrIIIC1_{Nme} bound to the HNH domain of NmeCas9. The overall structure shows that AcrIIIC1 binds directly to the HNH active site (Figure 4A), restricting it from accessing the target DNA. AcrIIIC1 binds to the active site interface of the HNH domain through several ionic and hydrogen-bonding interactions. Critically, the HNH domain active site residues H588 and D587 hydrogen bond to AcrIIIC1 residue S78 and to the backbone amine of C79, respectively (Figure 4B), possibly excluding the divalent cation necessary for target-strand DNA cleavage (Jinek et al., 2012). Mapping amino acid conservation onto the structure revealed that residues within the binding interface of both the HNH domain and AcrIIIC1 are highly conserved (Figures 4D, S4A, and S4B). In contrast to this observed conservation,

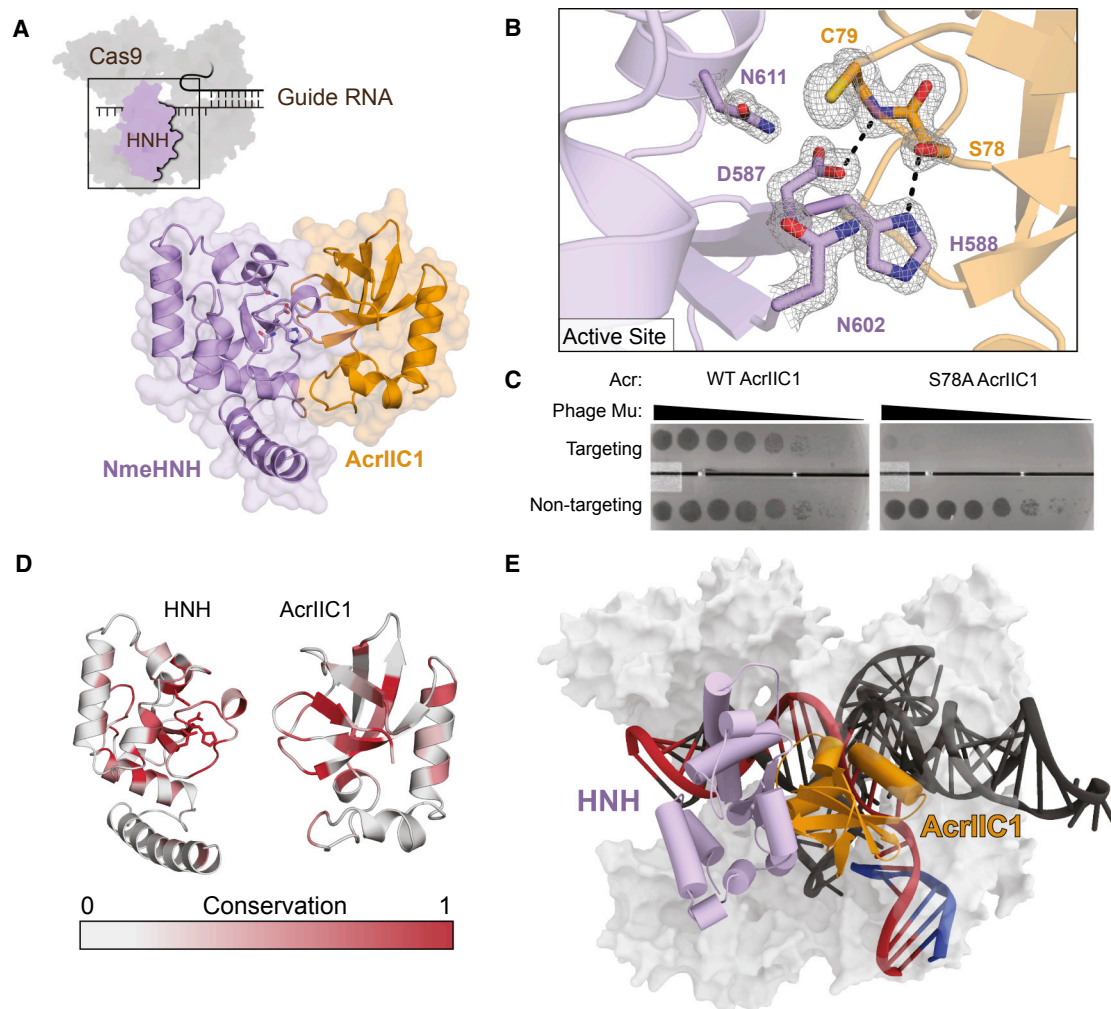


Figure 4. Structure of AcrIIC1 Bound to the NmeCas9 HNH Domain

(A) (Top) Cartoon depiction of NmeCas9 (gray) bound to a guide RNA (black). The black outline of the HNH domain (purple) indicates the binding interface to AcrIIC1. (Bottom) Crystal structure of NmeCas9 HNH domain bound to AcrIIC1 (PDB: 5VGB) is shown. Catalytic residues are depicted as sticks.

(B) Occlusion of HNH active site residues (purple) through hydrogen bonding with AcrIIC1 (orange). HNH catalytic residues H588 and D587 form hydrogen bonds (black dotted line) with S78 and the backbone amine of C79 of AcrIIC1, respectively. $2mF_o - DF_c$ electron density map is shown for interacting residues and contoured at 1.8σ .

(C) Plaques of *E. coli* phage Mu targeted by GeoCas9 in the presence of wild-type AcrIIC1 or the S78A AcrIIC1 mutant. Mutation of S78A results in nearly complete inactivation of AcrIIC1's inhibitory effect on GeoCas9.

(D) Binding interfaces of NmeCas9 HNH domain and AcrIIC1 show residue conservation. Conservation was calculated using multiple sequence alignments of AcrIIC1 orthologs and Cas9 HNH domains. Conserved residues are colored red (1, 100% sequence identity), and non-conserved residues are colored white (0). (E) Model of AcrIIC1 inhibiting cleavage of both target and non-target strands. NmeCas9 HNH domain (purple) was modeled into a "docked" position using dsDNA-bound SpyCas9 structure (PDB: 5F9R) as a reference for a homology model of NmeCas9. Placement of AcrIIC1 (orange) between the HNH domain and the target strand (red) prevents target cleavage and activation of the RuvC domain for non-target strand (dark blue) cleavage.

See also [Figures S4](#) and [S5](#) and [Table S1](#).

antagonistic binding interfaces often evolve rapidly, leading to lower conservation ([Franzosa and Xia, 2011](#)), suggesting that AcrIIC1 is targeting a highly conserved surface in order to limit the chance for the host to escape inhibition.

Comparative structural homology searches of AcrIIC1 against protein structure databases using DALI and Vast revealed that AcrIIC1 adopts a novel protein fold ([Holm and Laakso, 2016](#)). The $\beta_1\beta_2\beta_3\alpha_1\alpha_2\beta_4\beta_5$ fold of AcrIIC1 comprises a five-stranded

beta bundle interspaced by two alpha-helices. The beta bundle is the conserved core feature found in all AcrIIC1 orthologs whereas the internal loops connecting beta-strands and alpha-helices vary in length and composition across species ([Figure S4B](#)). All of the HNH-interacting residues occur within these variable loop regions, revealing how AcrIIC1 can evolve to target divergent HNH domains without compromising structural integrity.

For AcrIIC1 to effectively prevent Cas9 from cleaving the invading viral DNA, it must remain bound to the HNH domain for extended periods of time. This stable interaction is in part accomplished by multiple charged residues around the periphery of the active site that form an additional five hydrogen bonds with AcrIIC1 (Figure S4C). Interestingly, some interactions target conserved residues present in diverse Cas9 orthologs and other interactions appear to have evolved to target specific species. For example, S78 and E81 of AcrIIC1_{Nme} interact with the highly conserved catalytic residues H588 and N616 of the HNH_{Nme} domain, respectively. By contrast, AcrIIC1_{Nme} residue D14 and the backbone carbonyl of P39 interact with K551 and K549 of NmeCas9, which are mutated to a serine and glycine in AnaCas9. To assess the importance of individual amino acids for the biological function of AcrIIC1, we established an in vivo anti-CRISPR activity assay in *E. coli*. Plasmid-mediated expression of GeoCas9 and an sgRNA designed to target *E. coli* phage Mu (Morgan et al., 2002) led to a reduction in the plaquing efficiency of this phage by approximately 10⁶-fold (Figure 4C). Co-expression of wild-type AcrIIC1 restored the full plaquing activity of phage Mu, implying that GeoCas9 was completely inhibited by the anti-CRISPR. By contrast, the S78A mutant displayed very little anti-CRISPR activity in this assay, as phage Mu plaquing in the presence of this mutant was barely above background (Figures 4C and S4D). Substitutions of other residues positioned in the HNH:AcrIIC1 interaction interface, such as M76 and E81, caused more modest reductions in anti-CRISPR activity (Figure S4D) whereas substitution of other interface residues caused no reduction in biological activity. Importantly, all mutant proteins were expressed at the same level as wild-type (Figure S4E). AcrIIC1-interacting residues on the active site interface of the NmeCas9 HNH domain closely align with those on the same interface of *S. aureus* Cas9 (SauCas9) but diverge from equivalent residues in SpyCas9 and AnaCas9 mainly near the N terminus of the HNH domain (Figure S5A). Together with this structure, the high degree of structural similarity between the HNH domains of these species will enable rational engineering of AcrIIC1 to target specific Cas9 orthologs of interest.

Investigation of Cas9 target recognition and cleavage has uncovered several checkpoints along the interference pathway that ensure cleavage of the correct DNA sequence (Sternberg et al., 2015). The best understood of these checkpoints is mediated by the HNH domain, which undergoes a large rotation and translation to cleave the target DNA only when sufficient complementarity to the guide RNA is sensed (Dagdas et al., 2017; Sternberg et al., 2015). The structure presented here suggests that AcrIIC1 exploits one checkpoint in this process to ensure inhibited cleavage of both the target and non-target DNA strands. When modeled into a Cas9-sgRNA complex bound to double-stranded DNA (dsDNA) (Jiang et al., 2016), AcrIIC1 sterically blocks the HNH domain from rotating into position above the scissile phosphate (Figures 4E and S5B). We propose that the inability to correctly dock the HNH domain in the presence of AcrIIC1 inhibits RuvC cleavage of the non-target strand, explaining how a small protein that allows dsDNA engagement can still inhibit the two separate nucleases of Cas9.

AcrIIC3 Blocks DNA Binding and Induces NmeCas9 Dimerization

In contrast to AcrIIC1, AcrIIC3 has few natural orthologs and is found only in *Neisseria*. In HEK293T cells, expression of AcrIIC3 leads to the inability of dNmeCas9 to localize to a genomic target (Pawluk et al., 2016b), suggesting that AcrIIC3 prevents NmeCas9 from binding to DNA. We tested this biochemically using fluorescence polarization, which detected an ~10-fold decrease in equilibrium DNA binding affinity of NmeCas9 in the presence of AcrIIC3 (71 ± 13.4 nM without AcrIIC3 versus 859 ± 149 nM with AcrIIC3; Figure 5A). This reduced, but not abolished, binding affinity of NmeCas9 for DNA in the presence of AcrIIC3 may indicate that NmeCas9 can still interact with the PAM region of the DNA but cannot achieve complete R-loop formation (Mekler et al., 2017).

After incubating NmeCas9 and AcrIIC3 together, we noted a large shift in elution volume by size-exclusion chromatography (SEC) compared to either AcrIIC1-bound NmeCas9 or NmeCas9 alone (Figure 5B). This large shift suggested either a substantial conformational change or oligomerization of Cas9. Analysis of the fractions by small-angle X-ray scattering (SAXS) revealed that the AcrIIC3-bound NmeCas9 increased in size relative to NmeCas9 alone or NmeCas9-AcrIIC1, as indicated by an elongated pair distance distribution, increased radius of gyration (R_g), and volume of correlation (V_c) (Figures 5C and S6A). Using the power-law relationship for protein SAXS (Rambo and Tainer, 2013), we estimated the mass of NmeCas9 alone and AcrIIC1-bound NmeCas9 to be ~110 kDa, a slight underestimate of the theoretical masses of 124 kDa and 137 kDa, respectively. In contrast, the estimated mass of AcrIIC3-bound NmeCas9 was ~210 kDa. Together, our solution studies suggest that AcrIIC3 induces dimerization of NmeCas9, possibly contributing to its ability to block DNA binding. Analysis of AcrIIC3 alone by SEC and native mass spectrometry suggested that this Acr is monomeric in solution (Figures S6B and S6C), although dimerization of two AcrIIC3 monomers upon binding to NmeCas9 is possible.

To visualize the dimerization of NmeCas9, we examined NmeCas9 and AcrIIC3-bound NmeCas9 using electron microscopy. Although the protein interaction surfaces could not be identified due to limited resolution, an overall shape of the AcrIIC3-bound NmeCas9 complex can be observed in the 2D class averages (Figure 5D). To obtain better-resolution 2D class averages, the particles were cross-linked to reduce the flexibility of the NmeCas9-sgRNA complex and reduce dissociation of the dimer. These data reveal an overall symmetrical complex with dimensions consistent with two Cas9 proteins (Figure 5D). Cas9 inhibition by AcrIIC3-induced dimerization is consistent with the independent evolution of Acrs that act by diverse mechanisms.

DISCUSSION

We investigated the functions of two anti-CRISPR proteins, AcrIIC1 and AcrIIC3, and found that they block Cas9 activity by distinct mechanisms (Figure 6). AcrIIC1, an 85-amino-acid protein, inactivates a wide range of type IIC Cas9 orthologs by binding to and conformationally restraining the conserved HNH domain. The direct interaction with essential catalytic residues

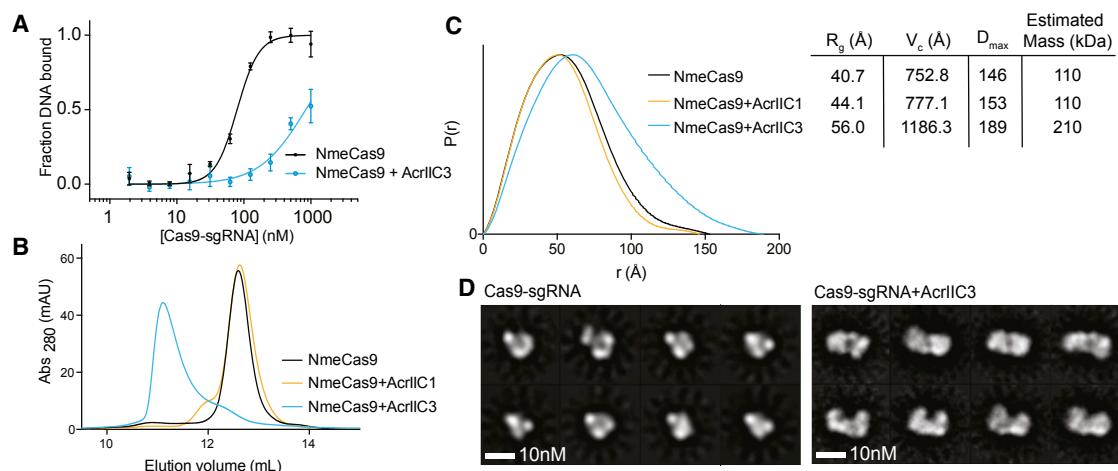


Figure 5. AcrIIC3 Blocks DNA Binding and Dimerizes Cas9

(A) Equilibrium binding measurements of NmeCas9 to dsDNA using fluorescence polarization in the presence (blue) or absence (black) of AcrIIC3. Measurements were made in triplicate, and the mean \pm SD is shown.

(B) Elution from a Superdex 200 10/300 size exclusion column for NmeCas9 (black), NmeCas9+AcrIIC1 (orange), and NmeCas9+AcrIIC3 (blue) showing a large shift in elution volume for NmeCas9-AcrIIC3, indicative of oligomerization.

(C) SAXS data for fractions collected from samples in (C). (Left) Pair-distance distribution function for NmeCas9 alone (black), with AcrIIC1 (orange) or with AcrIIC3 (blue), indicating increased particle size upon AcrIIC3 binding is shown. R_g , radius of gyration; V_c , volume of correlation; D_{max} , maximum dimension.

(D) 2D class averages of NmeCas9-sgRNA monomers (left) and NmeCas9-sgRNA bound to AcrIIC3 (right). The scale bar represents 10 nm.

See also Figures S2 and S6.

of the HNH domain limits the opportunity for Cas9 to mutate and escape inhibition by AcrIIC1, explaining the phylogenetic propagation of this inhibitor to target multiple Cas9 orthologs. Intriguingly, AcrIIC1 traps Cas9 in an inactive but DNA-bound state, effectively converting wild-type Cas9 into a catalytically inactive dCas9. In contrast, the 116-amino-acid AcrIIC3 binds specifically to the NmeCas9 enzyme to trigger dimerization and prevent DNA binding. Both of these mechanisms are different from that of the anti-CRISPR protein AcrIIA4, which acts as a DNA mimetic that prevents DNA binding by occupying the PAM-recognition site within a small subset of related type IIA Cas9 orthologs (Dong et al., 2017; Shin et al., 2017).

The CRISPR inhibition mechanisms determined in this study concur with two general strategies observed previously for blocking interference proteins in both type I and type II CRISPR systems. The first and most common mechanism is to target the CRISPR surveillance complex by disrupting DNA binding (AcrIIC3, AcrIIA4, AcrF1, and AcrF2; Bondy-Denomy et al., 2015; Chowdhury et al., 2017; Dong et al., 2017; Pawluk et al., 2016b; Rauch et al., 2017; Shin et al., 2017). The second is to target nucleases or nuclease domains, thereby allowing DNA binding, but not cleavage (AcrIIC1 and AcrF3; Bondy-Denomy et al., 2015; Wang et al., 2016). Of the currently studied Acrs, the strategy of inhibiting CRISPR RNA (crRNA) assembly with Cas proteins has yet to be found. The absence of this mechanism is possibly because this strategy would be unable to interfere with CRISPR nucleases that were assembled prior to infection. Nonetheless, many CRISPR systems are tightly regulated and are often activated in response to cell density and other factors (Høyland-Kroghsbo et al., 2017; Patterson et al., 2016, 2017). Inhibition of crRNA binding could be an effective Acr

method to inhibit those systems where RNP assembly coincides with phage infection, and such inhibitors may yet be discovered. Moreover, only Acrs that target CRISPR interference proteins have been found, despite the fact that the methods currently used to identify Acrs are capable of finding inhibitors of spacer acquisition and crRNA processing. Nonetheless, it is likely that, in cases where interference proteins are linked to other steps in CRISPR adaptive immunity, such as acquisition for type IIA Cas9 or RNA processing for Cas12a, such Acrs exist (Fonfara et al., 2016; Heler et al., 2015; Wei et al., 2015).

The mechanism of HNH domain binding by AcrIIC1 is particularly interesting for several reasons. First, the high structural similarity of the Cas9 HNH domain across Cas9 orthologs implies that AcrIIC1-type inhibitors may be more widespread than current analysis has identified. There also may be other Acrs that have converged on this mechanism. Second, type IIC Cas9 orthologs are capable of transactivating CRISPR RNA (tracrRNA)- and PAM-independent DNA cleavage of single-stranded DNA catalyzed by the HNH domain (Ma et al., 2015; Zhang et al., 2015). In addition to inhibition of double-stranded DNA cleavage, AcrIIC1 would also be able to inhibit this single-stranded cleavage activity, whereas inhibitors of PAM binding, such as AcrIIA4, may not be able to. Third, the fact that AcrIIC1 traps Cas9-guide RNA complexes in a catalytically inactive but DNA-bound state is consistent with additional roles for this inhibitor that include gene regulation rather than genome protection. Notably, efforts to engineer regulatory forms of Cas9 have utilized dCas9, a catalytically inactive mutant of the enzyme that retains RNA-programmed DNA binding activity. It would be exciting to determine whether bacteria natively employ AcrIIC1 to repurpose Cas9 as a gene regulator in cells. Whether or not

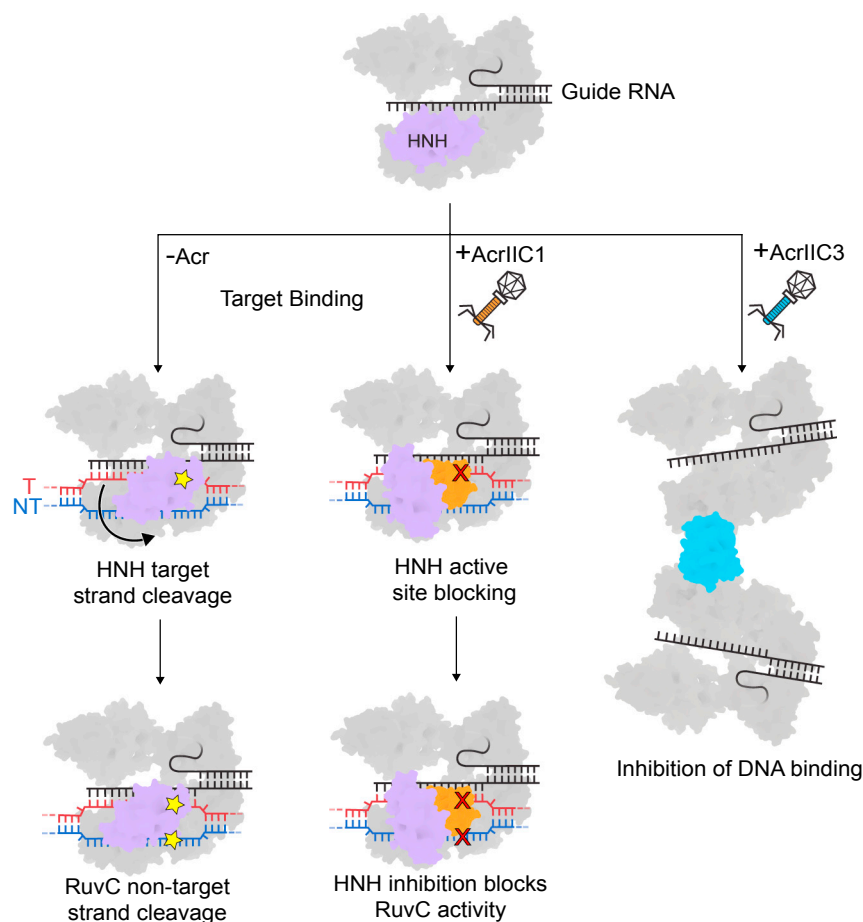


Figure 6. Model of AcrIIIC1 and AcrIIIC3 Inhibition of Cas9

Cas9 assembles with its guide RNA to form the search complex. Phage-encoded AcrIIIC1 (orange) binds to Cas9, still allowing target dsDNA binding but occluding the HNH (purple) active site and stopping cleavage of the target strand. AcrIIIC1 also conformationally restricts HNH docking, stopping cleavage on the non-target strand. For AcrIIIC3 (blue), Cas9's target DNA binding is inhibited and Cas9 is caused to dimerize.

this occurs in nature, it is an enticing possibility that AcrIIIC1 can be employed in gene-editing applications to obviate the need to generate separate dCas9 enzymes for gene-regulatory purposes (Gilbert et al., 2014; Mali et al., 2013; Qi et al., 2013). Finally, we note that the HNH fold is not unique to Cas9 but is in fact common to many bacterial restriction enzymes (Vasu and Nagaraja, 2013). This raises the possibility that, in addition to targeting CRISPR-based adaptive immunity, AcrIIIC1 also inhibits restriction enzymes. In line with this hypothesis, we observed that no Cas9 ortholog is present in *Pseudoaltermonas lipolytica* despite the presence of an AcrIIIC1. A blastp search of the *P. lipolytica* genome for Cas9 revealed an HNH restriction enzyme with homology to the Cas9 HNH domain (20% sequence identity of HNH domains). It may be that AcrIIIC1 has evolved to inhibit both adaptive (CRISPR) and innate (restriction) immune systems by targeting this conserved protein domain.

Given the rapid evolution and resourcefulness of phage, it is likely that Acrs are much more widespread than is currently known. As the toolbox of proteins used to edit genomes continues to expand to include other class 2 CRISPR systems, discovery of new Acrs can serve as potent tools to control these new systems. Continued analysis of the abundance of Acrs as well as their mechanisms will provide unique opportunities to regulate and disable CRISPR systems and in

the process illuminate the influence of Acrs on CRISPR diversity.

STAR★METHODS

Detailed methods are provided in the online version of this paper and include the following:

- KEY RESOURCES TABLE
- CONTACT FOR REAGENT AND RESOURCE SHARING
- EXPERIMENTAL MODELS AND SUBJECT DETAILS
 - *Escherichia coli* BL21 (DE3)
 - HEK293T
- METHOD DETAILS
 - Phylogenetic analyses
 - Protein expression and purification
 - Cleavage assays
 - HEK293T transfection and indel analysis
 - Filter binding
 - Gel shift assays and Fluorescence polarization
 - Isothermal titration calorimetry
 - Size exclusion binding assays
 - In vivo assay of AcrIIIC1 activity
 - Generation of AcrIIIC1 mutants

- Crystallography
- Small-angle X-ray scattering
- Electron microscopy

SUPPLEMENTAL INFORMATION

Supplemental Information includes six figures and one table and can be found with this article online at <http://dx.doi.org/10.1016/j.cell.2017.07.037>.

AUTHOR CONTRIBUTIONS

L.B.H., K.W.D., E.M., K.L.M., J.A.D., and A.R.D. designed experiments. L.B.H., A.E., N.A., and E.J.S. designed and performed cell-based assays. L.B.H., K.W.D., J.S.C., and J.C.C. purified proteins. L.B.H. designed and purified RNA and DNA substrates. L.B.H. and E.M. conducted in vitro cleavage and binding experiments. K.W.D. and E.M. assembled complex and set trays for protein crystallization. K.W.D. and L.B.H. acquired diffraction data. P.J.K. and K.W.D. determined the experimental phases of crystallographic data and traced the initial models, and K.W.D. completed model building. L.B.H. and G.J.K. conducted and analyzed SAXS experiments. J.-J. L. conducted electron microscopy experiments. A.R.D., K.L.M., and B.G. designed and executed phage-plaques experiments. L.B.H., K.W.D., and J.A.D. wrote the manuscript. All authors revised and agreed to the final manuscript. E.J.S. is a co-founder and scientific advisor of Intellia Therapeutics. J.A.D. is executive director of the Innovative Genomics Institute at the University of California, Berkeley and the University of California, San Francisco. J.A.D. is a co-founder of Editas Medicine, Intellia Therapeutics, and Caribou Biosciences and a scientific adviser to Caribou, Intellia, eFFECTOR Therapeutics and Driver. The Regents of the University of California have patents pending for CRISPR technologies on which the authors are inventors. The University of Toronto and the University of Massachusetts Medical School have patents pending for anti-CRISPR technologies on which the authors are inventors.

ACKNOWLEDGMENTS

We thank G. Meigs and the 8.3.1 beamline staff at the Advanced Light Source for assistance with data collection and members of the Doudna laboratory for comments and discussions. The 8.3.1 beamline is supported by UC Office of the President, Multicampus Research Programs and Initiatives grant MR-15-328599 and Program for Breakthrough Biomedical Research, which is partially funded by the Sandler Foundation. J.A.D. is an Investigator of the Howard Hughes Medical Institute. This research was supported in part by the Allen Distinguished Investigator Program, through The Paul G. Allen Frontiers Group, the National Science Foundation (MCB-1244557 to J.A.D.), the NIH (GM115911 to E.J.S.), and the Canadian Institutes of Health Research (MOP-130482 to A.R.D. and MOP-136845 to K.L.M.). L.B.H., K.W.D., and J.S.C. are supported by US National Science Foundation graduate research.

Received: May 16, 2017

Revised: June 29, 2017

Accepted: July 21, 2017

Published: August 24, 2017

REFERENCES

- Adams, P.D., Afonine, P.V., Bunkóczi, G., Chen, V.B., Davis, I.W., Echols, N., Headd, J.J., Hung, L.W., Kapral, G.J., Grosse-Kunstleve, R.W., et al. (2010). PHENIX: a comprehensive Python-based system for macromolecular structure solution. *Acta Crystallogr. D Biol. Crystallogr.* **66**, 213–221.
- Barrangou, R., Fremaux, C., Deveau, H., Richards, M., Boyaval, P., Moineau, S., Romero, D.A., and Horvath, P. (2007). CRISPR provides acquired resistance against viruses in prokaryotes. *Science* **315**, 1709–1712.
- Bondy-Denomy, J., Pawluk, A., Maxwell, K.L., and Davidson, A.R. (2013). Bacteriophage genes that inactivate the CRISPR/Cas bacterial immune system. *Nature* **493**, 429–432.
- Bondy-Denomy, J., Garcia, B., Strum, S., Du, M., Rollins, M.F., Hidalgo-Reyes, Y., Wiedenheft, B., Maxwell, K.L., and Davidson, A.R. (2015). Multiple mechanisms for CRISPR-Cas inhibition by anti-CRISPR proteins. *Nature* **526**, 136–139.
- Brouns, S.J., Jore, M.M., Lundgren, M., Westra, E.R., Slijkhuys, R.J., Snijders, A.P., Dickman, M.J., Makarova, K.S., Koonin, E.V., and van der Oost, J. (2008). Small CRISPR RNAs guide antiviral defense in prokaryotes. *Science* **321**, 960–964.
- Burstein, D., Harrington, L.B., Strutt, S.C., Probst, A.J., Anantharaman, K., Thomas, B.C., Doudna, J.A., and Banfield, J.F. (2017). New CRISPR-Cas systems from uncultivated microbes. *Nature* **542**, 237–241.
- Chowdhury, S., Carter, J., Rollins, M.F., Golden, S.M., Jackson, R.N., Hoffmann, C., Nosaka, L., Bondy-Denomy, J., Maxwell, K.L., Davidson, A.R., et al. (2017). Structure reveals mechanisms of viral suppressors that intercept a CRISPR RNA-guided surveillance complex. *Cell* **169**, 47–57.e11.
- Chylinski, K., Makarova, K.S., Charpentier, E., and Koonin, E.V. (2014). Classification and evolution of type II CRISPR-Cas systems. *Nucleic Acids Res.* **42**, 6091–6105.
- Dagdas, Y.S., Chen, J.S., Sternberg, S.H., Doudna, J.A., and Yildiz, A. (2017). A conformational checkpoint between DNA binding and cleavage by CRISPR-Cas9. *bioRxiv*. <http://dx.doi.org/10.1101/122242>.
- Dong, D., Guo, M., Wang, S., Zhu, Y., Wang, S., Xiong, Z., Yang, J., Xu, Z., and Huang, Z. (2017). Structural basis of CRISPR-SpyCas9 inhibition by an anti-CRISPR protein. *Nature* **546**, 436–439.
- Emsley, P., and Cowtan, K. (2004). Coot: model-building tools for molecular graphics. *Acta Crystallogr. D Biol. Crystallogr.* **60**, 2126–2132.
- Esvelt, K.M., Mali, P., Braff, J.L., Moosburner, M., Yaung, S.J., and Church, G.M. (2013). Orthogonal Cas9 proteins for RNA-guided gene regulation and editing. *Nat. Methods* **10**, 1116–1121.
- Fonfara, I., Le Rhun, A., Chylinski, K., Makarova, K.S., Lécrivain, A.-L., Bzdrenga, J., Koonin, E.V., and Charpentier, E. (2014). Phylogeny of Cas9 determines functional exchangeability of dual-RNA and Cas9 among orthologous type II CRISPR-Cas systems. *Nucleic Acids Res.* **42**, 2577–2590.
- Fonfara, I., Richter, H., Bratović, M., Le Rhun, A., and Charpentier, E. (2016). The CRISPR-associated DNA-cleaving enzyme Cpf1 also processes precursor CRISPR RNA. *Nature* **532**, 517–521.
- Franzosa, E.A., and Xia, Y. (2011). Structural principles within the human-virus protein-protein interaction network. *Proc. Natl. Acad. Sci. USA* **108**, 10538–10543.
- Garneau, J.E., Dupuis, M.-É., Villion, M., Romero, D.A., Barrangou, R., Boyaval, P., Fremaux, C., Horvath, P., Magadán, A.H., and Moineau, S. (2010). The CRISPR/Cas bacterial immune system cleaves bacteriophage and plasmid DNA. *Nature* **468**, 67–71.
- Gasiunas, G., Barrangou, R., Horvath, P., and Siksnys, V. (2012). Cas9-crRNA ribonucleoprotein complex mediates specific DNA cleavage for adaptive immunity in bacteria. *Proc. Natl. Acad. Sci. USA* **109**, E2579–E2586.
- Gilbert, L.A., Horlbeck, M.A., Adamson, B., Villalta, J.E., Chen, Y., Whitehead, E.H., Guimaraes, C., Panning, B., Ploegh, H.L., Bassik, M.C., et al. (2014). Genome-scale CRISPR-mediated control of gene repression and activation. *Cell* **159**, 647–661.
- Hale, C.R., Zhao, P., Olson, S., Duff, M.O., Graveley, B.R., Wells, L., Terns, R.M., and Terns, M.P. (2009). RNA-guided RNA cleavage by a CRISPR RNA-Cas protein complex. *Cell* **139**, 945–956.
- Harrington, L., Paez-Espino, D., Chen, J.S., Ma, E., Staahl, B.T., Kyrpides, N.C., and Doudna, J.A. (2017). A thermostable Cas9 with increased lifetime in human plasma. *bioRxiv*. <http://dx.doi.org/10.1101/138867>.
- Heler, R., Samai, P., Modell, J.W., Weiner, C., Goldberg, G.W., Bikard, D., and Marraffini, L.A. (2015). Cas9 specifies functional viral targets during CRISPR-Cas adaptation. *Nature* **519**, 199–202.
- Holm, L., and Laakso, L.M. (2016). Dali server update. *Nucleic Acids Res.* **44**, W351–W355.
- Hou, Z., Zhang, Y., Propson, N.E., Howden, S.E., Chu, L.-F., Sontheimer, E.J., and Thomson, J.A. (2013). Efficient genome engineering in human pluripotent

- stem cells using Cas9 from *Neisseria meningitidis*. *Proc. Natl. Acad. Sci. USA* 110, 15644–15649.
- Hoyland-Kroghsbo, N.M., Paczkowski, J., Mukherjee, S., Broniewski, J., Westra, E., Bondy-Denomy, J., and Bassler, B.L. (2017). Quorum sensing controls the *Pseudomonas aeruginosa* CRISPR-Cas adaptive immune system. *Proc. Natl. Acad. Sci. USA* 114, 131–135.
- Jiang, F., Taylor, D.W., Chen, J.S., Kornfeld, J.E., Zhou, K., Thompson, A.J., Nogales, E., and Doudna, J.A. (2016). Structures of a CRISPR-Cas9 R-loop complex primed for DNA cleavage. *Science* 351, 867–871.
- Jinek, M., Chylinski, K., Fonfara, I., Hauer, M., Doudna, J.A., and Charpentier, E. (2012). A programmable dual-RNA-guided DNA endonuclease in adaptive bacterial immunity. *Science* 337, 816–821.
- Kabsch, W. (2010). XDS. *Acta Crystallogr. D Biol. Crystallogr.* 66, 125–132.
- Kim, E., Koo, T., Park, S.W., Kim, D., Kim, K., Cho, H.Y., Song, D.W., Lee, K.J., Jung, M.H., Kim, S., et al. (2017). In vivo genome editing with a small Cas9 orthologue derived from *Campylobacter jejuni*. *Nat. Commun.* 8, 14500.
- Konarev, P.V., Volkov, V.V., Sokolova, A.V., Koch, M.H.J., and Svergun, D.I. (2003). *PRIMUS*: a Windows PC-based system for small-angle scattering data analysis. *J. Appl. Cryst.* 36, 1277–1282.
- Konarev, P.V., Petoukhov, M.V., Volkov, V.V., and Svergun, D.I. (2006). *ATSAS 2.1*, a program package for small-angle scattering data analysis. *J. Appl. Cryst.* 39, 277–286.
- Lander, G.C., Stagg, S.M., Voss, N.R., Cheng, A., Fellmann, D., Pulokas, J., Yoshioka, C., Irving, C., Mulder, A., Lau, P.W., et al. (2009). Appion: an integrated, database-driven pipeline to facilitate EM image processing. *J. Struct. Biol.* 166, 95–102.
- Lin, S., Staahl, B.T., Alla, R.K., and Doudna, J.A. (2014). Enhanced homology-directed human genome engineering by controlled timing of CRISPR/Cas9 delivery. *eLife* 3, e04766.
- Liu, J.J., Bratkowski, M.A., Liu, X., Niu, C.Y., Ke, A., and Wang, H.W. (2014). Visualization of distinct substrate-recruitment pathways in the yeast exosome by EM. *Nat. Struct. Mol. Biol.* 21, 95–102.
- Ma, E., Harrington, L.B., O'Connell, M.R., Zhou, K., and Doudna, J.A. (2015). Single-stranded DNA cleavage by divergent CRISPR-Cas9 enzymes. *Mol. Cell* 60, 398–407.
- Makarova, K.S., Wolf, Y.I., Alkhnbashi, O.S., Costa, F., Shah, S.A., Saunders, S.J., Barrangou, R., Brouns, S.J., Charpentier, E., Haft, D.H., et al. (2015). An updated evolutionary classification of CRISPR-Cas systems. *Nat. Rev. Microbiol.* 13, 722–736.
- Mali, P., Aach, J., Stranges, P.B., Esvelt, K.M., Moosburner, M., Kosuri, S., Yang, L., and Church, G.M. (2013). CAS9 transcriptional activators for target specificity screening and paired nickases for cooperative genome engineering. *Nat. Biotechnol.* 31, 833–838.
- Marraffini, L.A., and Sontheimer, E.J. (2008). CRISPR interference limits horizontal gene transfer in staphylococci by targeting DNA. *Science* 322, 1843–1845.
- Mekler, V., Minakhin, L., and Severinov, K. (2017). Mechanism of duplex DNA destabilization by RNA-guided Cas9 nuclease during target interrogation. *Proc. Natl. Acad. Sci. USA* 114, 5443–5448.
- Morgan, G.J., Hatfull, G.F., Casjens, S., and Hendrix, R.W. (2002). Bacteriophage Mu Genome Sequence: Analysis and Comparison with Mu-like Prophages in *Haemophilus* (*Neisseria* and *Deinococcus*).
- Núñez, J.K., Kranzusch, P.J., Noeske, J., Wright, A.V., Davies, C.W., and Doudna, J.A. (2014). Cas1-Cas2 complex formation mediates spacer acquisition during CRISPR-Cas adaptive immunity. *Nat. Struct. Mol. Biol.* 21, 528–534.
- Patterson, A.G., Jackson, S.A., Taylor, C., Evans, G.B., Salmond, G.P.C., Przybilski, R., Staals, R.H.J., and Fineran, P.C. (2016). Quorum sensing controls adaptive immunity through the regulation of multiple CRISPR-Cas systems. *Mol. Cell* 64, 1102–1108.
- Patterson, A.G., Yevstigneyeva, M.S., and Fineran, P.C. (2017). Regulation of CRISPR-Cas adaptive immune systems. *Curr. Opin. Microbiol.* 37, 1–7.
- Pawluk, A., Bondy-Denomy, J., Cheung, V.H.W., Maxwell, K.L., and Davidson, A.R. (2014). A new group of phage anti-CRISPR genes inhibits the type I-E CRISPR-Cas system of *Pseudomonas aeruginosa*. *mBio* 5, e00896-14.
- Pawluk, A., Staals, R.H.J., Taylor, C., Watson, B.N.J., Saha, S., Fineran, P.C., Maxwell, K.L., and Davidson, A.R. (2016a). Inactivation of CRISPR-Cas systems by anti-CRISPR proteins in diverse bacterial species. *Nat. Microbiol.* 1, 16085.
- Pawluk, A., Amrani, N., Zhang, Y., Garcia, B., Hidalgo-Reyes, Y., Lee, J., Edraki, A., Shah, M., Sontheimer, E.J., Maxwell, K.L., et al. (2016b). Naturally occurring off-switches for CRISPR-Cas9. *Cell* 167, 1829–1838.e9.
- Qi, L.S., Larson, M.H., Gilbert, L.A., Doudna, J.A., Weissman, J.S., Arkin, A.P., and Lim, W.A. (2013). Repurposing CRISPR as an RNA-guided platform for sequence-specific control of gene expression. *Cell* 152, 1173–1183.
- Rambo, R.P., and Tainer, J.A. (2013). Accurate assessment of mass, models and resolution by small-angle scattering. *Nature* 496, 477–481.
- Rauch, B.J., Silvis, M.R., Hultquist, J.F., Waters, C.S., McGregor, M.J., Krogan, N.J., and Bondy-Denomy, J. (2017). Inhibition of CRISPR-Cas9 with bacteriophage proteins. *Cell* 168, 150–158.e10.
- Semenyuk, A.V., and Svergun, D.I. (1991). *GNOM* - a program package for small-angle scattering data processing. *J. Appl. Cryst.* 24, 537–540.
- Shin, J., Jiang, F., Liu, J.-J., Bray, N.L., Rauch, B.J., Baik, S.H., Nogales, E., Bondy-Denomy, J., Corn, J.E., and Doudna, J.A. (2017). Disabling Cas9 by an anti-CRISPR DNA mimic. *Sci. Adv.* 3, e1701620.
- Shmakov, S., Smargon, A., Scott, D., Cox, D., Pyzocha, N., Yan, W., Abudayyeh, O.O., Gootenberg, J.S., Makarova, K.S., Wolf, Y.I., et al. (2017). Diversity and evolution of class 2 CRISPR-Cas systems. *Nat. Rev. Microbiol.* 15, 169–182.
- Stamatakis, A. (2014). RAxML version 8: a tool for phylogenetic analysis and post-analysis of large phylogenies. *Bioinformatics* 30, 1312–1313.
- Sternberg, S.H., LaFrance, B., Kaplan, M., and Doudna, J.A. (2015). Conformational control of DNA target cleavage by CRISPR-Cas9. *Nature* 527, 110–113.
- Terwilliger, T.C. (1999). Reciprocal-space solvent flattening. *Acta Crystallogr. D Biol. Crystallogr.* 55, 1863–1871.
- van Houte, S., Ekroth, A.K.E., Broniewski, J.M., Chabas, H., Ashby, B., Bondy-Denomy, J., Gandon, S., Boots, M., Paterson, S., Buckling, A., and Westra, E.R. (2016). The diversity-generating benefits of a prokaryotic adaptive immune system. *Nature* 532, 385–388.
- Vasu, K., and Nagaraja, V. (2013). Diverse functions of restriction-modification systems in addition to cellular defense. *Microbiol. Mol. Biol. Rev.* 77, 53–72.
- Wang, X., Yao, D., Xu, J.G., Li, A.R., Xu, J., Fu, P., Zhou, Y., and Zhu, Y. (2016). Structural basis of Cas3 inhibition by the bacteriophage protein AcrF3. *Nat. Struct. Mol. Biol.* 23, 868–870.
- Wei, Y., Terns, R.M., and Terns, M.P. (2015). Cas9 function and host genome sampling in Type II-A CRISPR-Cas adaptation. *Genes Dev.* 29, 356–361.
- Yamada, M., Watanabe, Y., Gootenberg, J.S., Hirano, H., Ran, F.A., Nakane, T., Ishitani, R., Zhang, F., Nishimasu, H., and Nureki, O. (2017). Crystal structure of the minimal Cas9 from *Campylobacter jejuni* reveals the molecular diversity in the CRISPR-Cas9 systems. *Mol. Cell* 65, 1109–1121.e3.
- Zhang, Y., Rajan, R., Seifert, H.S., Mondragón, A., and Sontheimer, E.J. (2015). DNase H activity of *Neisseria meningitidis* Cas9. *Mol. Cell* 60, 242–255.

STAR★METHODS

KEY RESOURCES TABLE

REAGENT or RESOURCE	SOURCE	IDENTIFIER
Bacterial and Virus Strains		
<i>Escherichia coli</i> BL21 (DE3)	J. Doudna Lab	N/A
<i>Escherichia coli</i> W, Mach1	J. Doudna Lab	N/A
<i>Escherichia coli</i> BB101	A. Davidson Lab	N/A
Chemicals, Peptides, and Recombinant Proteins		
Terrific Broth (TB)	VWR	Cat#J869-5kg
DMEM (Medium for mammalian cell culture)	Thermo Fisher Scientific	Cat#11965092
Penicillin-Streptomycin (For mammalian cell culture)	Thermo Fisher Scientific	Cat#10378016
Tobacco Etch Virus (TEV) protease	J. Doudna Lab	N/A
Gibson Assembly Master mix	New England Biolabs	Cat#E2611L
BfuAI	New England Biolabs	Cat#R0701L
High Fidelity 2 × PCR Master Mix	New England Biolabs	Cat#M0492L
T7 Endonuclease I	New England Biolabs	Cat#M0302L
OMEM	Thermo Fisher Scientific	Cat#31985070
SYBR gold	Thermo Fisher Scientific	Cat#S11494
Coomassie r-250	Thermo Fisher Scientific	Cat#20278
Ammonium sulfate	Sigma-Aldrich	Cat#A4915
Sodium acetate	Sigma-Aldrich	Cat#S2889
PEG 4000	Fluka	Cat#81240
Tris	J.T. Baker	Cat#4099-06
Imidazole	Sigma-Aldrich	Cat#I202
TCEP	Gold Biotechnology	Cat#TCEP25
PMSF	Sigma-Aldrich	Cat#P7626
Sodium chloride	J.T. Baker	Cat#4058-07
HEPES	EMD Millipore	Cat#5330
Glycerol	VWR	Cat#Bdh1172-4lp
Potassium chloride	Sigma-Aldrich	Cat#P9541
Magnesium chloride	Sigma-Aldrich	Cat#M2670
DTT	Gold Biotechnology	Cat#DTT100
ATP, [γ - 32 P]	PerkinElmer	Cat#NEG002A001MC
Igepal CA-630	Sigma-Aldrich	Cat#I8896
yeast tRNA	Thermo Fisher Scientific	Cat#AM7119
BSA	Sigma-Aldrich	Cat#A-7030
Heparin	Sigma-Aldrich	Cat#H-4784
Tween-20	Sigma-Aldrich	Cat#PC949
Iptg	Sigma-Aldrich	Cat#I2481C100
Critical Commercial Assays		
Ni-NTA agarose resin	QIAGEN	Cat#1018401
MBPTrap HP column	GE Healthcare	● Cat#28918779
HiTrap Heparin HP column	GE Healthcare	Cat#17-0406-01
Superdex 200 10/300 column	GE Healthcare	Cat#28990944
Superdex 75 10/300 column	GE Healthcare	Cat#29148721
Superdex75 16/600 column	GE Healthcare	Cat#28989333

(Continued on next page)

Continued

REAGENT or RESOURCE	SOURCE	IDENTIFIER
Easy-Xtal 15-well trays	QIAGEN	Cat#132006 and Cat#132008
DNeasy Blood and Tissue kit	QIAGEN	Cat#69504
Lipofectamine 2000	ThermoFisher Scientific	Cat#11668027
Quick Extraction Solution	Epicenter	Cat#QE09050
Deposited Data		
Coordinates of Nme Cas9 HNH and AcrIIC1	This paper	PDB: 5VGB
Experimental Models: Cell Lines		
Human: HEK293T		
Oligonucleotides		
DNMT1 Amplification F CCTCACACAACAGCTTCATGTCAGC	Integrated DNA Technologies	N/A
DNMT1 Amplification R GCCAAAGCCCGAGAGAGTGCC	Integrated DNA Technologies	N/A
TS2 Fwd GTTGGTCCTGAGTTCTAACTTTGGC	Integrated DNA Technologies	N/A
TS2 Rev AAAAGGTCAGCCTGGTAGACAGGG	Integrated DNA Technologies	N/A
TS6 Fwd TGCTTTCTTTGCCTGGACAC	Integrated DNA Technologies	N/A
TS6 Rev CCTCTCTGGCTCCATCGTAA	Integrated DNA Technologies	N/A
Nme FAM target T /56-FAM/TGGCTGTAAGCGGATGCCATA TGTGGGGATTCTGCCCCGCTT	Integrated DNA Technologies	N/A
Nme FAM target B AAGCGGGCAGAATCCCCACATATGGCA TCCGCTTACAGCC	Integrated DNA Technologies	N/A
Geo pUC Target T GCACGGTCACAGCTGGTCTGTAAGCGG ATGCCATATGTGGACAAACTG	Integrated DNA Technologies	N/A
Geo pUC Target B CAGTTTGTCCACATATGGCATCCGCTT ACAGACCAGCTGTGACCGTGC	Integrated DNA Technologies	N/A
Sequence Based reagents		
Geo NT sgRNA GGUCUGUAAGCGGAUGCCAUAUGGUCAUA GUUCCCCUGAgaauCAGGGUUACUAUGAU AAGGGCUUUCUGCCUAAGGCAGACUGACC CGCGGCGUUGGGGAUCGCCUGUCGCCCG CUUUUGGCGGGCAUCCCCAUCCUU	This paper	N/A
Geo DNMT1 sgRNA gGCAGCUGAGGCAGGUGCCUGCUGUCAUA GUUCCCCUGAgaauCAGGGUUACUAUGAU AAGGGCUUUCUGCCUAAGGCAGACUGACC CGCGGCGUUGGGGAUCGCCUGUCGCCCG CUUUUGGCGGGCAUCCCCAUCCUU	This paper	N/A
Geo pUC Target sgRNA GGUCUGUAAGCGGAUGCCAUAUGGUCAUA GUUCCCCUGAgaauCAGGGUUACUAUGAU AGGGCUUUCUGCCUAAGGCAGACUGACCCG CGGCGUUGGGGAUCGCCUGUCGCCCGCUU UUGGCGGGCAUCCCCAUCCUU	This paper	N/A

(Continued on next page)

Continued

REAGENT or RESOURCE	SOURCE	IDENTIFIER
Nme pUC Target sgRNA	This paper	N/A
GGUCUGUAAGCGGAUGCCAU AUGGUUG UAGCUCUUUCUCGAAAGAGAACCGU UGCUCACAAUAGGCCGUCUGAAAAGAUG UGCCGCAACGCUCUGCCCCUAAAGCU UCUGCUUUAACGGGCUUUUUUU		
Spy pUC Target sgRNA	This Paper	N/A
GGUCUGUAAGCGGA UGCCAU AUGGUUUUAGAG CUAGAAUAGCAAGUUA AAUAAGGCUAGUCCGUU AUCAACUUGAAAAGUGGCA CCGAGUCGGUGCUUUUUUU		
Cje pUC target sgRNA	This Paper	N/A
GGUCUGUAAGCGGAUG CCAU AUGGUUUUAGUCC CUGAAAAGGGACUAAAAU AAAGAGUUUGCGGGAC UCUGCGGGGUACAAU CCCCUAAAACCGCU UUUUU		
1NmeY13A	Integrated DNA Technologies	N/A
aaattggaataatgccgggGCtgatggctgcggtcttgc		
1NmeD42A	Integrated DNA Technologies	N/A
gcgacattgtcctgattacgCtggcgatgataaagctgagg		
1NmeD44A	Integrated DNA Technologies	N/A
ttgtcctgattacgatggcgCtgataaagctgaggattggc		
1NmeK46A	Integrated DNA Technologies	N/A
ctgattacgatggcgatgatGCagctgaggattggctgagat		
1NmeM76A	Integrated DNA Technologies	N/A
acgcataatcgtcggttggtGCggcctcatgttgggagttg		
1NmeS78A	Integrated DNA Technologies	N/A
atacgtcggttggtatggccGcatgttgggagttgtgaac		
1NmeC79A	Integrated DNA Technologies	N/A
cgtcggttggtatggcctcaGcttgggagttgtgaactaT		
1NmeW80A	Integrated DNA Technologies	N/A
cggttggtatggcctcatgtGCggagttgtgaactaTGAA		
1NmeE81A	Integrated DNA Technologies	N/A
ttggtatggcctcatgttgggCgtttgtgaactaTGAAGCT		
1NmeV83A	Integrated DNA Technologies	N/A
tggcctcatgttgggagttgCtgaactaTGAAGCTTG CGGC		
03Lys8F	Integrated DNA Technologies	N/A
TCCAaataacatggaactttgggtaG		
03Lys8R	Integrated DNA Technologies	N/A
ATGACTaccacaaagttccatgtatt		
Recombinant DNA		
pET-MBP-Geo_st	Addgene	87700
pET-MBP-NLS-Geo_st	Addgene	87703
pMJ839	Addgene	39317
pEJS427-pCSDest2-AcrE2	Addgene	85677

(Continued on next page)

Continued

REAGENT or RESOURCE	SOURCE	IDENTIFIER
pEJS430-pCSDest2-AcrIIIC1Boe	Addgene	85678
pEJS433-pCSDest2-AcrIIIC1Nme	Addgene	85679
pJH376	Addgene	86842
PX404 <i>Campylobacter jejuni</i> Cas9	Addgene	68338
pEJS469-pLK.O1-SpySgRNA/DTS13-Telomere	Addgene	85715
pCDF-1b	Novagen	71330-3
pGeoCas9-sgRNA	This work	https://benchling.com/s/seq-IXSEQMlloSlZmGtpNslid
Software and Algorithms		
RAxML		https://sco.h-its.org/exelixis/web/software/raxml/index.html
Prism		https://www.graphpad.com/scientific-software/prism/
Coot		https://www2.mrc-lmb.cam.ac.uk/personal/pemsley/coot/
Phenix		https://www.phenix-online.org/download/
Pymol		https://www.pymol.org/
SCATTER		http://www.bioisis.net/tutorial/9
ATSAS		https://www.embl-hamburg.de/biosaxs/download.html
PRIMUS		https://www.embl-hamburg.de/biosaxs/primus.html
GNOM		https://www.embl-hamburg.de/biosaxs/manuals/gnom.html
Appion		http://emg.nysbc.org/redmine/projects/appion/wiki/Appion_Home
MAFFT		http://mafft.cbrc.jp/alignment/software/
Other		
Tufryn	Pall	Cat#66228
Protran	GE Healthcare	Cat#10600000
Hybond-N+	GE Healthcare	Cat#RPN203-b

CONTACT FOR REAGENT AND RESOURCE SHARING

Please direct any requests for further information or reagents to the Lead Contact, Jennifer A. Doudna (doudna@berkeley.edu).

EXPERIMENTAL MODELS AND SUBJECT DETAILS***Escherichia coli* BL21 (DE3)**

E. coli BL21 (DE3) cells were used for protein expression for in vitro studies, crystallography, and RNP delivery for genome editing. Cells were grown at 18°C in Terrific Broth (TB) medium for 14 hr.

HEK293T

Cells were cultured at 37°C, 5% CO₂ in DMEM + 10% FBS + 1% Penicillin/Streptomycin.

METHOD DETAILS**Phylogenetic analyses**

Cas9 and Acr protein sequences were gathered from previous publications and additional Cas9 orthologs targeted by Acrs were added (Burstein et al., 2017; Fonfara et al., 2014; Pawluk et al., 2016b). A non-redundant set of proteins was compiled by clustering

proteins with > 90% identity. Proteins were aligned using MAFFT and maximum-likelihood phylogenies were constructed using RAxML (Stamatakis, 2014). Trees were visualized using FigTree 1.4.1.

Protein expression and purification

Proteins were purified as previously described (Jinek et al., 2012) with modification. For Cas9, *E. coli* BL21(DE3) was grown in Terrific Broth at 18°C for 14 hr. Cells were harvested and resuspended in Lysis Buffer (50 mM Tris-HCl, pH 7.5, 20 mM imidazole, 0.5 mM TCEP-NaOH, 500 mM NaCl and 1 mM PMSF), disrupted by sonication, and purified on Ni-NTA resin. TEV protease was incubated with the elution overnight at 4°C. Next, the protein was run over an MBP affinity column onto a heparin column and eluted with a gradient from 300–1250 mM NaCl. The resulting fractions containing Cas9 were purified using a Superdex 200 10/300 gel filtration column and flash frozen in Storage Buffer (20 mM HEPES-NaOH, pH 7.5, 5% (v/v) glycerol, 150 mM NaCl and 1 mM TCEP-NaOH). The HNH domain and Acrs were purified using the same procedure, omitting the heparin and MBP column.

Cleavage assays

All reactions were carried out in 1 × Reaction Buffer (20 mM Tris-HCl, pH 7.5, 100 mM KCl, 5 mM MgCl₂, 1 mM DTT and 5% glycerol (v/v)). 500 nM Cas9 was complexed with 625 nM sgRNA for 5 min at 37°C. The Acr was added at 2.5 μM and the reaction was incubated at 37°C for another 5 min. Next, DNA substrate was added to a final concentration of 25 nM and the reaction was allowed to react for 15 min (Figure 1A) or for 30 s, 1 min, 2 min, 5 min and 30 min (Figure S1B). Products were analyzed on 1.25% agarose, 0.5 × TAE gels stained with ethidium bromide.

For P32-labeled DNA cleavage assays, 40 nM Cas9 was complexed with 40 nM sgRNA in 1 × Reaction Buffer for 10 min at 37°C. The AcrIC1 was added at 400 nM and the reaction was incubated at room temperature for another 20 min. Next probe was added to a final concentration of ~1 nM and the reaction was allowed to react for 0, 1, 2.5, 5 and 10 min (Figure 2B). Products were analyzed on 12% denature PAGE gel before being dried and visualized by phosphorimaging.

HEK293T transfection and indel analysis

Plasmids expressing NmeCas9, SpyCas9 and their respective sgRNAs targeting the DTS3 site, as well as plasmids expressing AcrE2 (Addgene #85677), AcrIC1_{Boe} (Addgene #85678) and AcrIC1_{Nme} (Addgene #85679), were previously described (Pawluk et al., 2016a, 2016b). AcrIIA4 expressing plasmid (Addgene #86842) was described previously (Rauch et al., 2017). The CjeCas9-expressing plasmid (PX404) was acquired from Addgene (#68338). For CjeCas9 sgRNA expression, the published sgRNA sequence (Kim et al., 2017) was synthesized as a gBlock (IDT), and was used to replace the NmeCas9 sgRNA cassette in pLKO.1-puro plasmid [(Pawluk et al., 2016b); Addgene #85715] by Gibson Assembly. The resulting plasmid (pEJS676) contains the CjeCas9 sgRNA cassette with *Bfu*AI sites that can be used to insert any spacer of interest. Next, two previously validated guide sequences [targeting the AAVS1 locus (TS2 and TS6; (Kim et al., 2017))] were inserted into the CjeCas9 sgRNA expression construct, yielding plasmids pEJS677 and pEJS678, respectively.

Plasmids were used to transfect HEK293T cells as previously described (Pawluk et al., 2016b). Briefly, 1.5 × 10⁵ HEK293T cells [cultured at 37°C, 5% CO₂ in DMEM + 10% FBS + 1% Penicillin/Streptomycin (GIBCO)] were transiently transfected with 100 ng Cas9-expressing plasmid, 100 ng sgRNA-expressing plasmid, and 100 ng Acr plasmid. 72 hr after transfection, cells were harvested and genomic DNA was extracted with the DNeasy Blood and Tissue kit (QIAGEN). 50 ng genomic DNA was used for PCR amplification [High Fidelity 2 × PCR Master Mix (New England Biolabs)] with primers flanking the targeted site. The T7 Endonuclease I (T7E1, New England Biolabs) digestion was performed according to the manufacturer's instructions, and samples were fractionated in a 2.5% agarose/1 × TAE gel, and visualized by ImageQuant LAS 4000.

For GeoCas9 RNP, 20 pmol of RNP was assembled as previously described (Lin et al., 2014) and mixed with 10 μl OMEM. The RNP was added to 10 μl of 1:10 dilution of Lipofectamine 2000 (Life Technologies) in OMEM and allowed to incubate at room temperature for 10 min before adding it to the cells. The same procedure was used to deliver the indicated molar ratio of AcrIC1. For analysis of indels, genomic DNA was extracted using Quick Extraction Solution (Epicenter), and the *DNMT1* locus was amplified by PCR. T7E1 reactions were conducted according to the manufacturer's instructions and products were analyzed on a 1.5% agarose gel stained with SYBR gold (Thermo Fisher Scientific). Guide sequences and primers for amplification of targeted sites can be found in the Key Resources Table.

Filter binding

Filter binding assays were conducted as previously described (Ma et al., 2015). Assays were conducted in RNA Binding Buffer (20 mM Tris-HCl, pH 7.5, 150 mM KCl, 5 mM MgCl₂, 1 mM DTT, 5% (v/v) glycerol, 0.01% Igepal CA-630, 10 μg ml⁻¹ yeast tRNA, and 10 μg ml⁻¹ BSA). < 0.02 nM radiolabeled sgRNA was incubated with Cas9 at the specified concentration for 20 min and loaded onto a dot-blot apparatus through Tufryn, Protran and Hybond-N+ membranes, in that order. The membranes were washed with 50 μL Equilibration Buffer (20 mM Tris-HCl, pH 7.5, 150 mM KCl, 5 mM MgCl₂, 1 mM DTT, 5% glycerol) before being dried and visualized by phosphorimaging. Data were fit to a binding isotherm using Prism (GraphPad Software).

Gel shift assays and Fluorescence polarization

Electrophoretic mobility shift assays (EMSA) were conducted as previously described (Ma et al., 2015). Binding reactions were conducted in 1 × Binding Buffer (20 mM Tris-HCl, pH 7.5, 150 mM KCl, 5 mM EDTA, 5 mM MgCl₂, 1 mM DTT, 5% (v/v) glycerol, 50 μg ml⁻¹ heparin, 0.01% Tween 20, and 100 μg ml⁻¹ BSA). Cas9 and sgRNA were incubated first for 5 min at 37°C to allow for guide binding. Next the Cas9–sgRNA complex was diluted to the indicated concentration and a constant amount of 20 μM Acr was added to each sample and allowed to incubate for 10 min at room temperature. Radiolabeled DNA target was then added (< 0.05 nM). The binding reaction was incubated at 37°C for 30 min at room temperature. Samples were analyzed by 6% polyacrylamide/0.5 × TBE gel electrophoresis. Gels were dried and imaged by phosphorimaging. Assays were conducted in triplicate with representative gels shown. The same procedure was used for fluorescence polarization except that 10 nM FAM labeled probe was used in place of the radiolabeled DNA and binding was analyzed using fluorescence polarization.

Isothermal titration calorimetry

Isothermal titration calorimetry was conducted as previously described (Nuñez et al., 2014). Proteins were dialyzed overnight into 20 mM HEPES-NaOH, pH 7.5, 300 mM NaCl and 1 mM TCEP-NaOH. 100 μM AcrIIIC1 was titrated into the cell containing 10 μM NmeCas9. Origin software (OriginLab) was used for baseline correction, integration and curve fitting. The K_D reported is the mean ± standard deviation of three replicates.

Size exclusion binding assays

To test for binding, ~20 μM Cas9, Cas9 chimeras or Cas9 truncations were incubated with ~40 μM of Acr or Acr–GFP. Binding was conducted in Storage Buffer (above) omitting the glycerol. Complexes were resolved on either a Superdex 200 10/300 (full-length Cas9 and chimeras) or Superdex 75 10/300 (HNH domains). Fractions were analyzed on a 4%–20% PAGE gel and stained with Coomassie G-250.

In vivo assay of AcrIIIC1 activity

A plasmid expressing GeoCas9 targeting *E. coli* phage Mu was constructed from pGeoCas9–sgRNA. This plasmid was linearized with BsaI, and DNA encoding a crRNA targeting phage Mu was inserted (oligos 03Lys8F and 03Lys8R). AcrIIIC1 was expressed by synthesizing its gene (GenScript) and ligating it to vector, pCDF-1 digested with NcoI and HindIII.

The plasmid expressing the Mu-targeting GeoCas9 and the plasmid expressing WT or mutant AcrIIIC1 were co-transformed into *E. coli* strain BB101 (a derivative of BL21(DE3) with a deletion of the *slyD* gene). Cells carrying both plasmids were subcultured (1:100) in LB containing chloramphenicol and streptomycin, grown for 2 hr, and the AcrIIIC1 expression was induced with 0.01 mM IPTG. After 3 hr of induction, 200 μL of cells were mixed with top agar and poured onto LB agar plates containing both antibiotics, and supplemented with 200 ng/mL aTc (to induce GeoCas9), 0.2% arabinose and MgSO₄ (10 mM). Phage Mu lysates were spotted in 10-fold serial dilutions onto these plates after the top agar had hardened.

To confirm AcrIIIC1 mutant expression in *E. coli*, 500 μL of culture after IPTG induction was centrifuged, and then cells were resuspended in 100 μL SDS loading buffer. AcrIIIC1 mutant expression was analyzed by SDS-PAGE on a 15% Tris-Tricine gel, followed by Coomassie Blue staining.

Generation of AcrIIIC1 mutants

Mutations were introduced into the AcrIIIC1 open reading frame, contained in the pCDF-1b-derived plasmid by site-directed mutagenesis. For each mutation, two 40bp complementary primers containing the desired mutation in the center with correct sequences on both sides were designed (see Key Resources Table). The PCR reaction was conducted using Pfu DNA polymerase (Thermo-Scientific), followed by DpnI digestion to eliminate the wild-type plasmid. The resulting DNA product was used to transform *E. coli* Stellar cells (Clontech). Plasmids were isolated from streptomycin resistant colonies and all mutations were verified by sequencing.

Crystallography

Crystals were obtained by hanging-drop vapor diffusion at 18°C. Purified NmeCas9 HNH domain was incubated with a 1.2 × molar excess of AcrIIIC1_{Nme} on ice for 30 min. Complexed Nme HNH–AcrIIIC1 was separated over a Superdex75 16/600 column in gel filtration buffer (150 mM NaCl, 20 mM HEPES-NaOH pH 7.5, 0.5 mM TCEP-NaOH). Preliminary crystallization conditions were identified by sparse-matrix screen using 400 nL drops set over 70 μL reservoir solutions in a 96-well format (Falcon). Optimized crystals were grown in Easy-Xtal 15-well trays (QIAGEN) in 2 μL drops with a 1:1 ratio of protein and reservoir solution with a final protein concentration ~12 mg mL⁻¹ in 200 mM ammonium sulfate, 0.1 M sodium acetate pH 4.25, and 22% (w/v) PEG 4000.

Crystals were further optimized by micro-seeding to improve single crystal formation. Crystals were looped and crushed by vortexing and optimized in 2 μL hanging drops composed of 0.2 μL (1:10,000) micro-seed dilution, 1 μL of 7 mg mL⁻¹ protein complex, and 0.8 μL reservoir solution. Single crystals were transferred with a nylon loop to a new drop containing reservoir solution supplemented with 15% (v/v) glycerol as a cryoprotectant and incubated for approximately 30 s before flash freezing in liquid nitrogen. Native and anomalous data were collected under cryogenic conditions at the Lawrence Berkeley National Laboratory Advanced Light Source (Beamline 8.3.1).

X-ray diffraction data were processed with *XDS* and *AIMLESS* (Kabsch, 2010) using the SSRL *autoxds* script (A. Gonzalez, Stanford SSRL). Nme HNH-AcrIIC1 crystals belonged to the orthorhombic space group $P 2_1 2_1 2_1$, and contained one copy of each protein in the asymmetric unit. Sulfur single-wavelength anomalous dispersion (S-SAD) data were collected from a single native crystal for experimental phase determination. Briefly, iterative datasets were collected at $\sim 6,000$ V and merged until a potential phase solution was obtained at $\sim 90^\circ$ multiplicity using HySS in *PHENIX* (Adams et al., 2010). Manual placement of a orthologous HNH domain from *Actinomyces naeslundii* was used to confirm the resulting map and allow extension of the correct solution to the native data processed to ~ 1.50 Å using SOLVE/RESOLVE (Terwilliger, 1999). The correct phase solution contained 17 sites corresponding to 16 sulfur atoms and 1 SO_4 position. The Final model was completed by iterative model building in *COOT* (Emsley and Cowtan, 2004) and before refinement with *PHENIX*. X-ray data for refinement were extended according to an l/σ resolution cut-off of ~ 1.0 , CC^* correlation, R_{pim} parameters, and visual inspection of the resulting map.

Small-angle X-ray scattering

Small-angle X-ray scattering (SAXS) data were collected at the SIBYLS beamline at the Lawrence Berkeley National Laboratory Advanced Light Source. Data of NmeCas9, NmeCas9+Acr1 and NmeCas9+Acr3 was collected over a dilution series from 1 to 4 mg mL⁻¹.

Data were background-corrected in *SCATTER* (BIOISIS) before primary data processing using the *ATSAS* software package (Konarev et al., 2006). The Guinier region, intensity at 0 [$I(0)$], and radius of gyration (R_g) were calculated using *PRIMUS* (Konarev et al., 2003). The $P(r)$ distribution and maximum dimension (D_{max}) were calculated using *GNOM* (Semenyuk and Svergun, 1991). Molecular weights were calculated from the mass parameter Q_R in *SCATTER* using the volume-of-correlation (V_c) and the power-law relationship for protein (Rambo and Tainer, 2013).

Electron microscopy

NmeCas9-sgRNA-AcrIIC3 was cross-linked by 0.02% glutaraldehyde at room temperature for 7 min. NmeCas9-sgRNA was used directly after gel filtration. All samples were diluted to a final concentration of ~ 100 nM and negatively stained in 2% (w/v) uranyl acetate solution following the standard deep-stain procedure on holey carbon-coated EM copper grids covered with a thin layer of continuous carbon (Liu et al., 2014). Negatively stained specimens were mounted on a transmission electron microscope holder and examined by a Tecnai Spirit electron microscope operated at 120-kV acceleration voltage. Magnified digital micrographs of the specimen were taken at a nominal magnification of 49,000 on a Gatan Ultrascan4000 CCD camera with a pixel size of 2.18 Å at the specimen level. The defocus values used were about -1.0 to -1.5 μm , and the total accumulated dose at the specimen was about 50 electrons per Å². The particle picking and 2D analysis were performed within Appion (Lander et al., 2009).

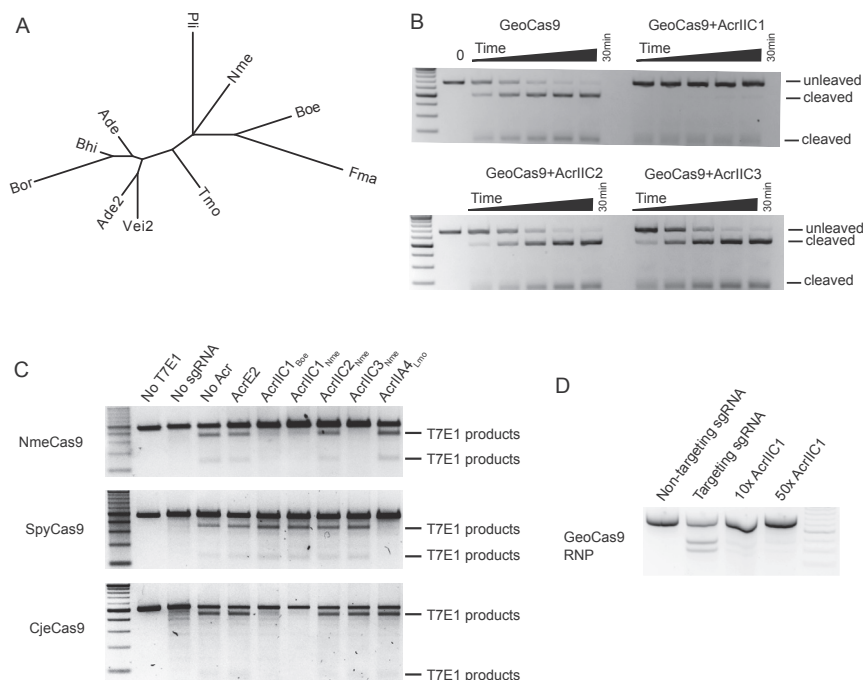


Figure S1. AcrIIC1 Inhibits Diverse Cas9 Orthologs, whereas AcrIIC2 and AcrIIC3 Are Highly Specific, Related to Figure 1

(A) Unrooted phylogenetic tree of AcrIIC1.

(B) Kinetic measurement of DNA cleavage mediated by GeoCas9 in the presence or absence of type IIC Acrs.

(C) Genome editing mediated by NmeCas9, SpyCas9 and CjeCas9 in the presence of various Acrs. Human (HEK293T) cells were transfected with plasmids expressing NmeCas9, SpyCas9, or CjeCas9, along with cognate, previously validated sgRNAs targeting genomic sites. T7E1 digestion was used to detect editing. A type I anti-CRISPR (AcrE2) was used as a negative control for inhibition. As reported previously, NmeCas9 genome editing (upper panel) was inhibited by AcrIIC1_{Boe}, AcrIIC1_{Nme}, and AcrIIC3_{Nme}; full inhibition by AcrIIC2_{Nme} in human cells generally requires higher amounts of cotransfected expression plasmid. Inhibition of SpyCas9 genome editing (middle panel) was observed only with AcrIIC4_{Lmo} (Rauch et al., 2017). In contrast, CjeCas9 editing activity (bottom panel) was inhibited by AcrIIC1_{Boe} and AcrIIC1_{Nme}, but not by any of the other anti-CRISPRs.

(D) GeoCas9 RNP mediated editing of HEK293T cells in the presence and absence of AcrIIC1. Indels were analyzed by T7E1 digestions.

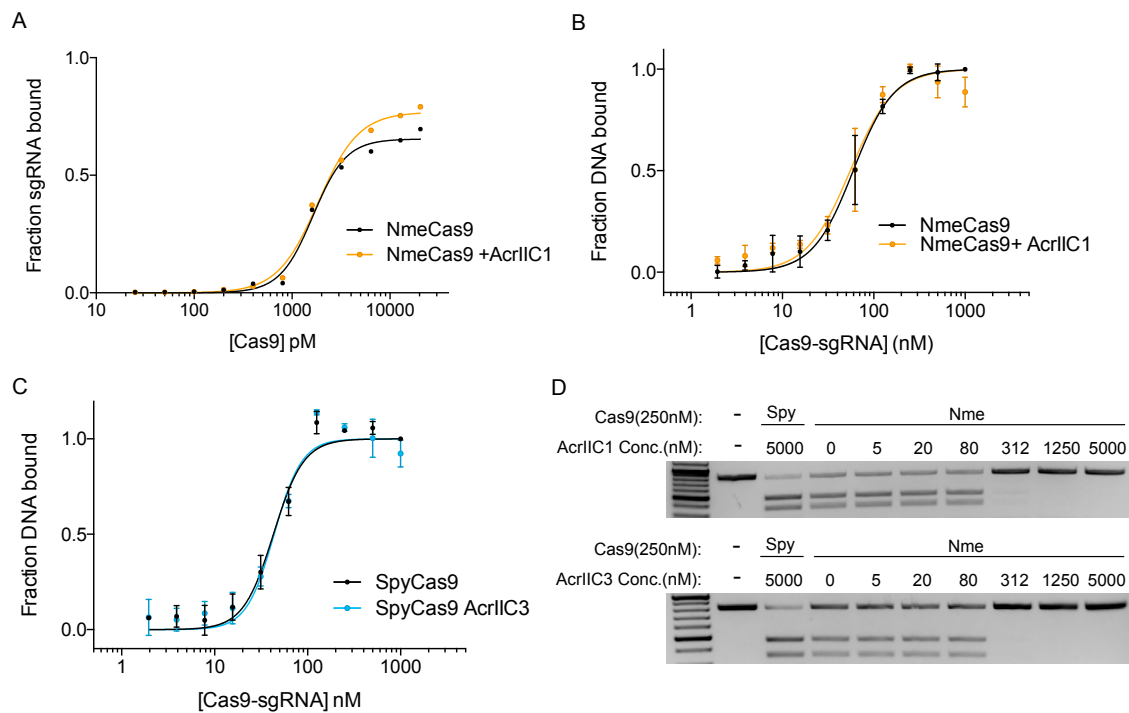


Figure S2. Impact of AcrIIC1 and AcrIIC3 on Cas9 RNA and DNA Binding, Related to Figures 2 and 5

(A) Filter-binding assays measuring the affinity of NmeCas9 to its guide in the presence and absence of AcrIIC1. Radiolabeled sgRNA was incubated with NmeCas9 in the presence (orange) or absence (black) of AcrIIC1. NmeCas9-sgRNA RNP formation was measured using a filter binding assay and fraction sgRNA bound was calculated and plotted against NmeCas9 concentration. When incubated with Cas9 prior to sgRNA binding, AcrIIC1 does not inhibit RNP formation. (B) Equilibrium binding measurements of NmeCas9-sgRNA binding to dsDNA in the presence and absence of AcrIIC1, measured by fluorescence polarization. (C) Equilibrium binding measurements of SpyCas9 in the presence and absence of AcrIIC3, related to Figure 5D. (D) DNA cleavage assays conducted by NmeCas9-sgRNA in the presence of increasing concentrations of AcrIIC1 and AcrIIC3.

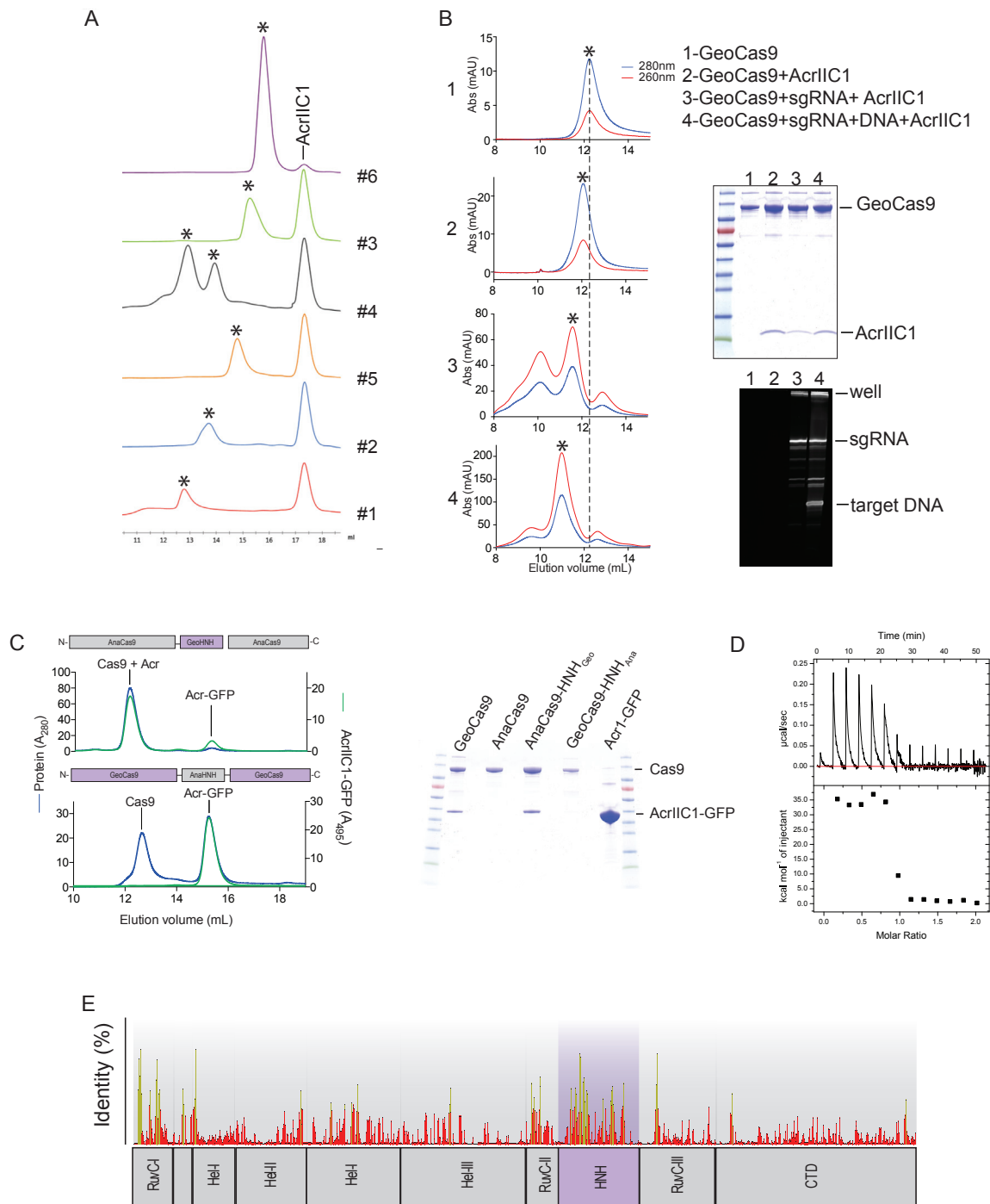


Figure S3. AcrIIC1 Binds to the Cas9 HNH Domain, Related to Figure 3

(A) Superdex 200 10/300 traces of truncations used to identify the binding interface of AcrIIC1. Each trace included the indicated GeoCas9 truncation and excess AcrIIC1. Black asterisks indicate the fractions analyzed in Figure 3B. For construct #4 (REC lobe), multiple peaks resulted from bound contaminating nucleic acid species from the purification and both peaks were pooled and analyzed together.

(B) Superdex 200 10/300 traces for GeoCas9 complexed with the components indicated in the top right. Fractions indicated with asterisk were analyzed on SDS-PAGE gel (upper gel) and denaturing urea PAGE gel (lower gel) and components were added in the order listed.

(1, Apo GeoCas9; 2, GeoCas9+AcrIIC1; 3, GeoCas9+sgRNA+AcrIIC1; 4, GeoCas9+sgRNA+DNA+AcrIIC1).

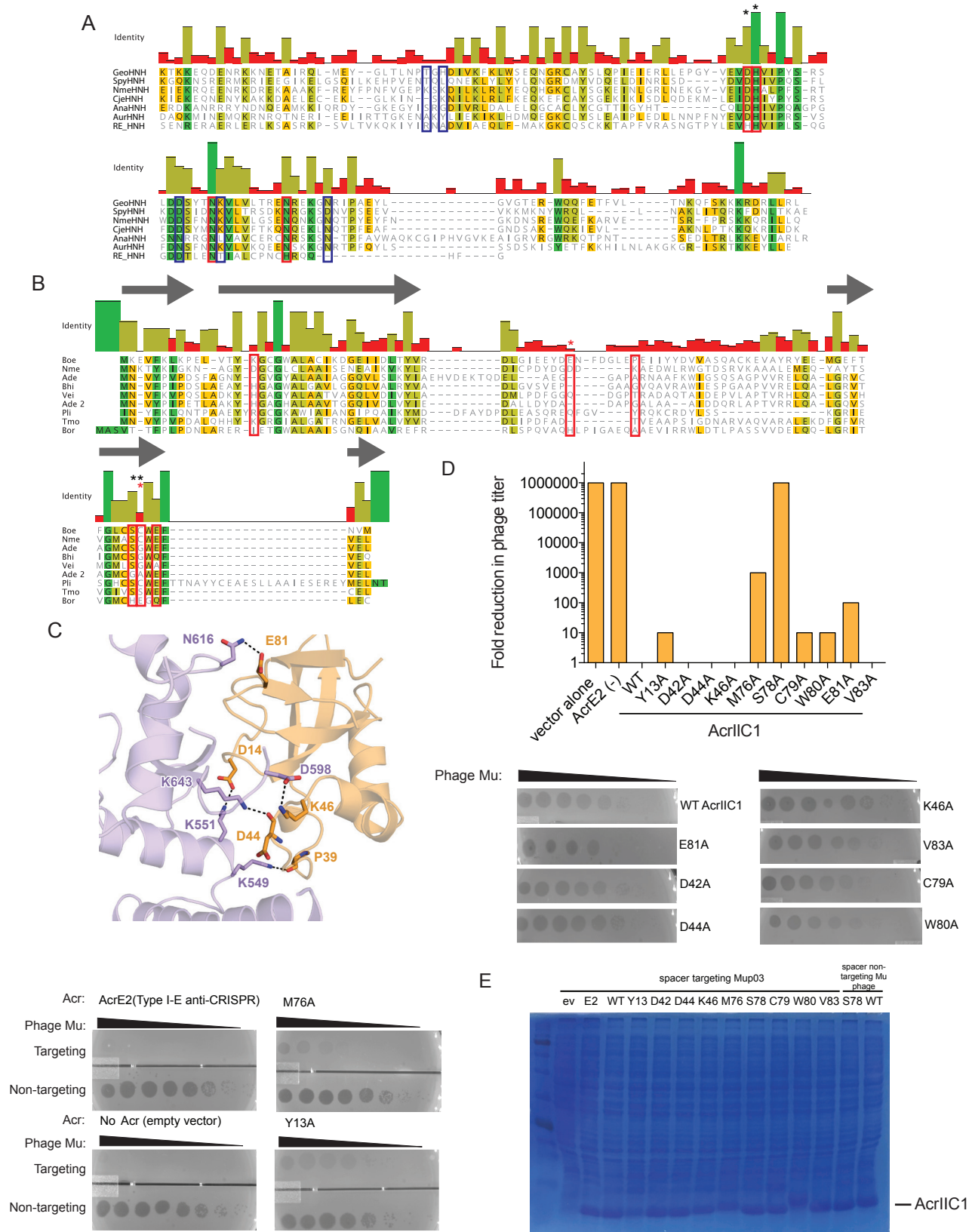
(C) (top) HNH domains between GeoCas9 (orange) and AnaCas9 (yellow) were swapped to create chimeric Cas9 proteins. AcrIIC1 was fused with GFP (to more easily visualize a change in elution volume once bound to Cas9) and run over a S200 size-exclusion column. Additionally, AcrIIC1-GFP detection at a wavelength

(legend continued on next page)

of 495 nm offers another indication of change in AcrIIIC1 elution volume. (bottom) SDS-PAGE gradient gel (4%–20%) with protein samples from S200 elution peaks of chimeric Cas9 proteins incubated with AcrIIIC1.

(D) Representative ITC trace for AcrIIIC1 binding to the NmeCas9 HNH domain.

(E) Conservation of Cas9 mapped onto the approximate domain boundaries below using a non-redundant list of Cas9 orthologs from all Cas9 subtypes. HNH is highlighted in purple. Bar heights are proportional to protein identity, with yellow bars indicating highly conserved residues.



(legend on next page)

Figure S4. Alignment of HNH Domains and AcrIIC1 Orthologs and Structure of AcrIIC1–HNH, Related to Figure 4

(A) A multiple sequence alignment of selected HNH domains. The multiple sequence alignment was generated using the extracted HNH domains of 6 Cas9 orthologs and the restriction enzyme from *Pseudomonas lipolytica* (RE_HNH). Red boxes surround catalytic residues and black asterisks indicate catalytic residues involved in AcrIIC1 binding. Blue boxes surround other residues involved in AcrIIC1 interaction.

(B) A multiple sequence alignment of AcrIIC1 using 11 AcrIIC1 orthologs. Highest degree of conservation occurs within a beta barrel (marked by a gray arrow). Red boxes surround selected residues involved in the binding between the NmeCas9 HNH domain and AcrIIC1_{Nme}. Red asterisks indicate AcrIIC1 residues that interact with the backbone of HNH. Black asterisks indicate AcrIIC1 residues that interact with catalytic residues of the HNH domain.

(C) Charged residues (depicted as sticks) surrounding the active site of the HNH domain (purple) form ionic and hydrogen binding interactions (depicted as dotted black lines) with AcrIIC1 (orange).

(D) Fold reduction in phage titer in response to GeoCas9 targeting of phage Mu in the presence of AcrIIC1 mutants. One representative plate is shown for each mutant tested. 10-fold serial dilutions of phage Mu lysate were spotted lawns of bacteria expressing the indicated AcrIIC1 mutant. The fold reductions shown in the bar graph were qualitatively evaluated from inspecting three replicates of each experiment.

(E) SDS-PAGE gel showing the expression levels of WT and mutant AcrIIC1s used for experiments in (D). The approximate mass of AcrIIC1 is indicated on the right (ev, empty vector; E2, AcrIIC2).

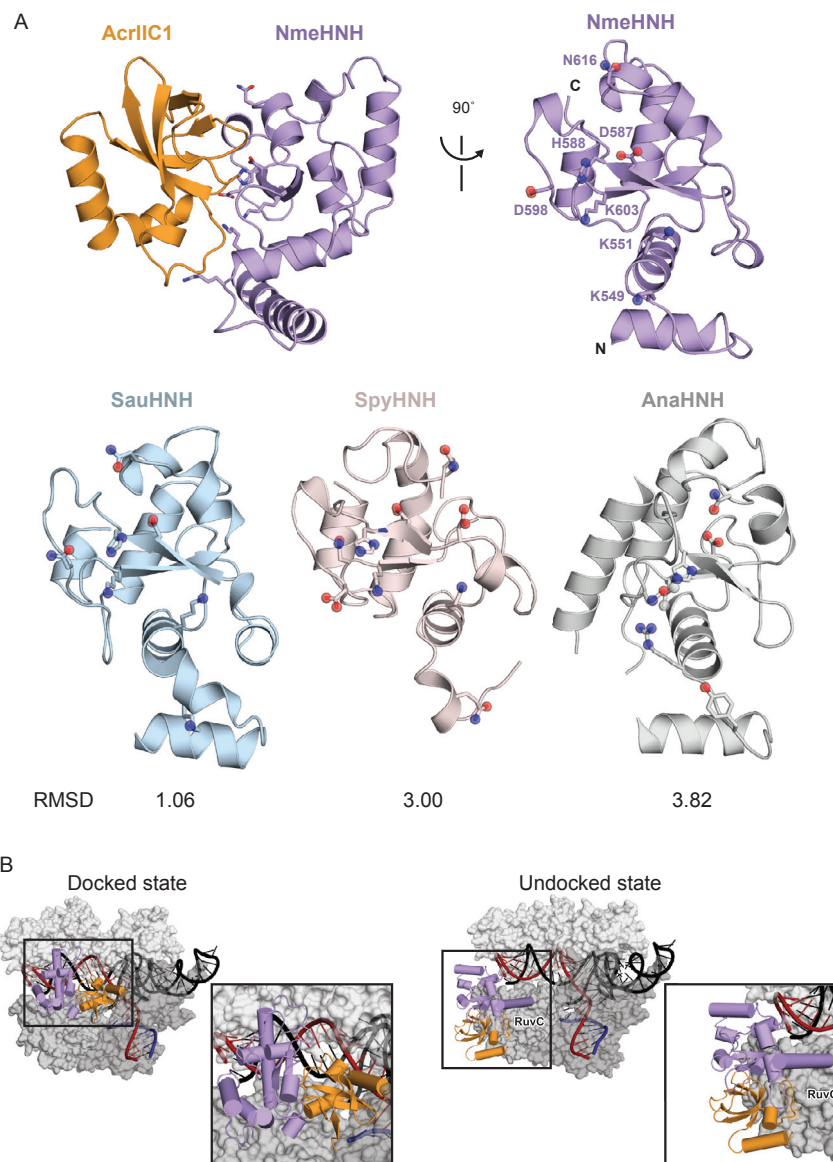


Figure S5. Conservation of the Cas9 HNH Domain in the Context of Full-Length Cas9, Related to Figure 4

(A) Crystal structure of NmeCas9 HNH domain bound to AcrIIIC1 (PDB: 5VGB). The HNH is rotated 90° C to show the active site interface with labeled residues (depicted as sticks) involved in AcrIIIC1 binding. (Bottom) Crystal structures of the HNH domains from three Cas9 orthologs (*Staphylococcus aureus*, PDB: 5CZZ; *Streptococcus pyogenes*, PDB: 4CMP; *Actinomyces naeslundii*, PDB: 4OGE). RMSD values were generated using super alignment in PyMol. Comparison of crystallized Cas9 orthologs reveals strong similarity between AcrIIIC1 interacting residues of NmeCas9 and SauCas9 HNH domains.

(B) (Left) Model of AcrIIIC1 inhibiting cleavage of both target and non-target strands. NmeCas9 HNH domain (purple) was modeled into a “docked” position using the dsDNA-bound SpyCas9 structure (PDB: 5F9R) as a reference. Placement of AcrIIIC1 (orange) between the HNH domain and the target strand (red) prevents target cleavage and activation of the RuvC domain for non-target strand (dark blue) cleavage. The black box shows a zoomed-in view of the NmeHNH-AcrIIIC1 complex. (Right) Model of AcrIIIC1 clashing with the RuvC domain when the HNH domain is in an “undocked” conformation. NmeCas9 HNH was placed in a undocked conformation using a GeoCas9 Phyre model as a reference. Placement of AcrIIIC1 indicates steric clashing with the RuvC domain, indicating that binding of AcrIIIC1 to the HNH domain must position the HNH domain between the docked and undocked positions. The black box shows a zoomed-in view of the HNH_{Nme}-AcrIIIC1_{Nme} complex.

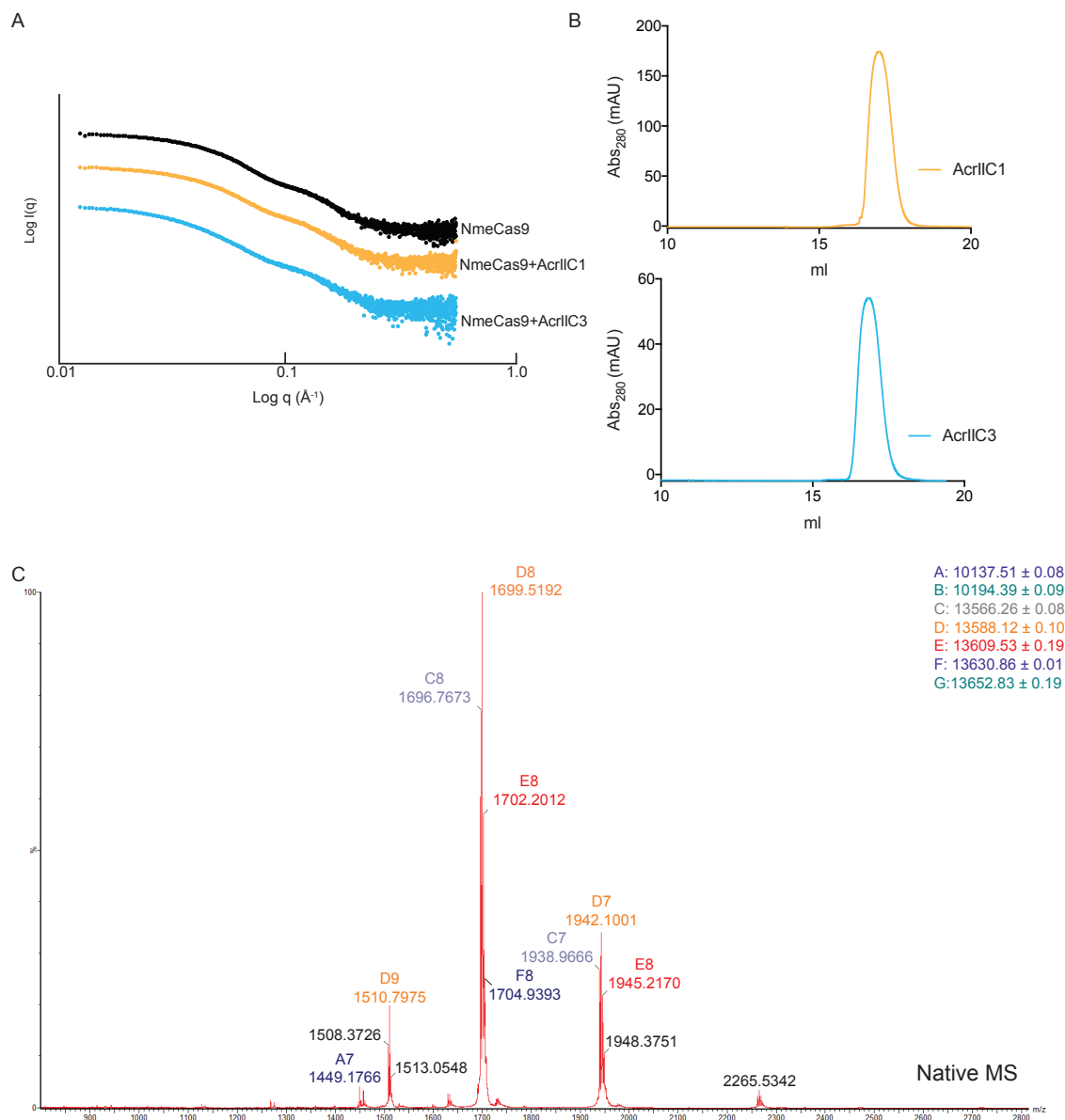


Figure S6. AcrIIIC3 Is Monomeric and Dimerizes NmeCas9, Related to Figure 5

(A) Small-angle X-ray scattering (SAXS) curves of NmeCas9, NmeCas9+AcrIIIC1 and AcrIIIC3.

(B) Analysis of AcrIIIC1 (yellow, top) and AcrIIIC3 (blue, bottom) on a Superdex 200 10/300 size exclusion column.

(C) Native mass spectrometry of AcrIIIC3. The estimated masses (Da) from deconvoluting the charge series are identified in the top right corner.